



**HAL**  
open science

## **Chromogranin A preferential interaction with Golgi phosphatidic acid induces membrane deformation and contributes to secretory granule biogenesis**

Ophélie Carmon, Fanny Laguerre, Lina Riachy, Charlène Delestre-Delacour, Qili Wang, Emeline Tanguy, Lydie Jeandel, Dorthe Cartier, Tamou Thahouly, Anne-Marie Haeberlé, et al.

### ► To cite this version:

Ophélie Carmon, Fanny Laguerre, Lina Riachy, Charlène Delestre-Delacour, Qili Wang, et al.. Chromogranin A preferential interaction with Golgi phosphatidic acid induces membrane deformation and contributes to secretory granule biogenesis. *FASEB Journal*, 2020, 34 (5), pp.6769-6790. <10.1096/fj.202000074R>. <hal-02525074>

**HAL Id: hal-02525074**

**<https://normandie-univ.hal.science/hal-02525074v1>**

Submitted on 9 Dec 2020

**HAL** is a multi-disciplinary open access archive for the deposit and dissemination of scientific research documents, whether they are published or not. The documents may come from teaching and research institutions in France or abroad, or from public or private research centers.

L'archive ouverte pluridisciplinaire **HAL**, est destinée au dépôt et à la diffusion de documents scientifiques de niveau recherche, publiés ou non, émanant des établissements d'enseignement et de recherche français ou étrangers, des laboratoires publics ou privés.



HAL Authorization

1 **Chromogranin A preferential interaction with Golgi phosphatidic acid induces**  
2 **membrane deformation and contributes to secretory granule biogenesis**

3  
4 Ophélie Carmon<sup>1†</sup>, Fanny Laguerre<sup>1†</sup>, Lina Riachy<sup>1†</sup>, Charlène Delestre-Delacour<sup>1£</sup>, Qili  
5 Wang<sup>2</sup>, Emeline Tanguy<sup>2</sup>, Lydie Jeandel<sup>1</sup>, Dorthé Cartier<sup>1</sup>, Tamou Thahouly<sup>2</sup>, Anne-Marie  
6 Haeberlé<sup>2</sup>, Laetitia Fouillen<sup>3</sup>, Olivier Rezazgui<sup>4</sup>, Damien Schapman<sup>5</sup>, Alexandre Haefel<sup>4</sup>,  
7 Yannick Goumon<sup>2</sup>, Ludovic Galas<sup>5</sup>, Pierre-Yves Renard<sup>4</sup>, Stéphane Alexandre<sup>6</sup>, Nicolas  
8 Vitale<sup>2§</sup>, Youssef Anouar<sup>1§</sup> and Maité Montero-Hadjadje<sup>1§\*</sup>

9  
10 <sup>1</sup> Normandie Univ, UNIROUEN, INSERM, U1239, Laboratoire de Différenciation et  
11 Communication Neuronale et Neuroendocrine, Institut de Recherche et d'Innovation  
12 Biomédicale de Normandie, 76000, Rouen, France

13 <sup>2</sup> Centre National de la Recherche Scientifique, Université de Strasbourg, Institut des  
14 Neurosciences Cellulaires et Intégratives, F-67000 Strasbourg, France

15 <sup>3</sup> Laboratoire de Biogénèse Membranaire, UMR-5200 CNRS, Plateforme Métabolome,  
16 Université de Bordeaux, 33883 Villenave D'Ornon, France

17 <sup>4</sup> Normandie Univ, UNIROUEN, COBRA, UMR 6014 and FR 3038, INSA Rouen, CNRS,  
18 76000 Rouen, France

19 <sup>5</sup> Normandie Univ, UNIROUEN, INSERM, PRIMACEN, 76000, Rouen, France

20 <sup>6</sup> Normandie Univ, UNIROUEN, CNRS, UMR 6270, Polymères, Biopolymères, Surfaces  
21 Laboratory, 76000, Rouen, France

22  
23 <sup>†</sup> These authors equally contributed to this work.

24 <sup>£</sup> Present address: Normandie Univ, UNIROUEN, Laboratoire GLYCOMÉV, Fédération de  
25 recherche Normandie-Végétal - FED 4277, GDR CNRS 3711 COSM'ACTIFS, 76000,  
26 Rouen, France

27 <sup>§</sup> These authors equally contributed to this work.

28 <sup>\*</sup> Corresponding author; Tel: +33 235146643; e-mail: maite.montero@univ-rouen.fr

29  
30 RUNNING TITLE: CgA/PA interaction and granulogenesis

31

32 NONSTANDARD ABBREVIATIONS

33

34 AFM: atomic force microscopy

35 CgA: chromogranin A

36 CgB: chromogranin B

37 DOPC: 1,2-dioleoyl-sn-glycero-3-phosphocholine

38 FIPI: 5-Fluoro-2-indolyl des-chlorohalopemide

39 gCW STED: time-gated continuous wave stimulated emission depletion

40 GUV: giant unilamellar vesicle

41 ITC: isothermal titration calorimetry

42 PA: phosphatidic acid

43 PABD: PA binding domain

44 PC: phosphatidylcholine

45 PE: phosphatidylethanolamine

46 PS: phosphatidylserine

47 PDE4A1: cAMP phosphodiesterase-4A1

48 PLD: phospholipase D

49 SgII: secretogranin II

50 Spo20p: Sporulation-specific protein 20

51 SUV: small unilamellar vesicle

52 TGN: *trans*-Golgi network

53 **ABSTRACT**

54 Chromogranin A (CgA) is a key luminal actor of secretory granule biogenesis at the *trans*-  
55 Golgi network level but the molecular mechanisms involved remain obscure. Here, we  
56 investigated the possibility that CgA acts synergistically with specific membrane lipids to  
57 trigger secretory granule formation. We show that CgA preferentially interacts with the  
58 anionic glycerophospholipid phosphatidic acid (PA). In accordance, bioinformatic analysis  
59 predicted a PA-binding domain (PABD) in CgA sequence that effectively bound PA (36:1) or  
60 PA (40:6) in membrane models. We identified PA (36:1) and PA (40:6) as predominant  
61 species in Golgi and granule membranes of secretory cells and we found that CgA interaction  
62 with these PA species promotes artificial membrane deformation and remodeling.  
63 Furthermore, we demonstrated that disruption of either CgA PABD or phospholipase D  
64 (PLD) activity significantly alters secretory granule formation in secretory cells. Our findings  
65 show for the first time the ability of CgA to interact with PLD-generated PA, which allows  
66 membrane remodeling and curvature, key processes necessary to initiate secretory granule  
67 budding.

68

69 **KEY WORDS:** membrane dynamics / organelle biogenesis / phospholipase D / Golgi  
70 apparatus

71

72

## 73 INTRODUCTION

74 Secretory granules are vesicular organelles which materialize the regulated secretory pathway,  
75 allowing release of signal molecules such as hormones and neurotransmitters from endocrine,  
76 neuroendocrine, and most neuronal cells. Secretory granules are formed by budding from the  
77 trans-Golgi network (TGN) membrane in a very efficient manner and more than several  
78 thousand can accumulate in neuroendocrine cells for active release upon cell stimulation,  
79 most likely involving a specific budding process from the Golgi apparatus (1). It is now well  
80 established that membrane remodeling at the TGN is an important process for secretory  
81 granule budding, but the identity of the molecular actors, the sequence of events, and the  
82 mechanisms involved are not elucidated to date.

83 The TGN membrane is composed of a broad spectrum of lipids with specific properties  
84 that profoundly define its identity and function (2), but their contribution to secretory granule  
85 biogenesis has only recently emerged. Membrane proteins are known to influence lipid  
86 organization and conversely protein function and clustering are also under the control of  
87 lipids, leading to the formation of TGN membrane microdomains that have been proposed to  
88 regulate the budding of secretory granules (3). For instance, *in vitro* and *in vivo* studies  
89 revealed that depletion of cholesterol alters secretory granule biogenesis (4, 5), and the  
90 regulated production and organization of sphingomyelin, which assembles with cholesterol to  
91 generate microdomains in the membranes, has been shown to be crucial for the biogenesis of  
92 cargo carriers at the Golgi membranes (6). Moreover, the TGN membrane cytosolic leaflet is  
93 highly enriched in phosphatidylinositol 4-phosphate (PI4P), which may directly induce  
94 membrane curvature and/or recruit membrane-deforming cytosolic PI4P-binding proteins (7).  
95 Thus, besides the TGN membrane components, cytosolic but also luminal molecular  
96 components potentially influence membrane organization and shape. Among the luminal  
97 components, several glycoproteins of the granin family were proposed to play a crucial role in  
98 secretory granule biogenesis (8). In particular, chromogranin A (CgA) was shown to  
99 contribute to hormone aggregation and secretory granule biogenesis (9–11). Indeed, deletion  
100 of the CgA gene (*Chga*) led to decreased secretory granule number associated to metabolic  
101 complications such as cardiovascular defects and obesity in knockout mice (12, 13), implying  
102 a major contribution of CgA in catecholamine and insulin storage and release. In previous  
103 studies, we have shown that ectopic CgA expression induced the formation of secretory  
104 granule-like structures in COS7 cells, which are normally devoid of secretory granules and  
105 granin expression (14, 15), confirming the important role of CgA in granulogenesis. These

106 observations suggested that CgA could act at the level of the TGN membrane to trigger the  
107 formation of secretory granules; however, the mechanism involved is still unknown.

108 The first indication for a role of CgA at the TGN level is related to its acidic nature  
109 which confers to this granin the ability to aggregate with neuropeptides and hormones in the  
110 luminal TGN condition (9). Besides these soluble aggregates, a fraction of CgA was found to  
111 be tightly associated with secretory granule membrane (16), suggesting that CgA/hormone  
112 aggregates might interact with the TGN membrane. Indeed, the conserved  $\alpha$ -helical  
113 organization of CgA terminal regions which confers to the protein the ability to trigger  
114 secretory granule formation and to sort hormones to the regulated secretory pathway (11, 14),  
115 the faculty of CgA to regulate fusion pore expansion (17) and the widespread expression of  
116 this granin argue for a role of CgA in granulogenesis through direct interaction with  
117 membranes. In fact, CgA-derived peptides with the conserved  $\alpha$ -helical conformation have  
118 been shown to interact with membrane lipids. For instance, the conserved N-terminal peptide  
119 of CgA named vasostatin I (hCgA1-76) interacts with phosphatidylserine in phospholipid  
120 monolayers (18) and cell surface (19), whereas the peptide catestatin (hCgA352-372) binds to  
121 phosphatidylcholine micelles (20). As it is now well established that lipid composition and  
122 properties define organelle identity and function, we explored the possibility that an  
123 interaction between CgA and specific lipids of the TGN membrane could promote secretory  
124 granule biogenesis. In this study, we observed that CgA interacts with phosphatidic acid (PA)  
125 and phosphoinositides in membrane models and that ectopic expression of a cytosolic probe  
126 which buffers Golgi PA in secretory cells impaired the formation of CgA-containing granules.  
127 Moreover, we found that CgA preferentially interacts with few PA species enriched in  
128 purified Golgi and secretory granule membranes *in vitro*, through a newly identified PA-  
129 binding domain (PABD). Using giant unilamellar vesicles (GUVs) enriched with Golgi and  
130 secretory granule PA species, we observed that CgA induces GUV membrane remodeling and  
131 deformation in a dose-dependent manner. Interestingly, deletion of the identified PABD in  
132 CgA significantly reduced secretory granule biogenesis. Finally, genetic and pharmacological  
133 evidence revealed that inhibition of phospholipase D (PLD), a major source of PA production  
134 in the Golgi, alters secretory granule formation in neuroendocrine cells.

135

136

## 137 **MATERIALS AND METHODS**

### 138 **Cell culture and transfection**

139 African green monkey kidney fibroblast-derived COS7 cells (American Type Culture  
140 Collection; CRL 1651), wild-type or stably expressing CgA developed previously (15) and  
141 mouse corticotrope-derived AtT20/DC16v-F2 cells (American Type Culture Collection; CRL  
142 1795) were maintained in Dulbecco's Modified Eagle's Medium (DMEM, Gibco, Thermo  
143 Fisher Scientific) supplemented with 5% heat-inactivated and sterile-filtered fetal bovine  
144 serum (FBS, Sigma - Aldrich), 100 U ml<sup>-1</sup> penicillin, 100 µg ml<sup>-1</sup> streptomycin (Gibco,  
145 Thermo Fisher Scientific) and 300 µg ml<sup>-1</sup> geneticin (G-418 sulfate, Life Technologies, Inc,  
146 UK) to maintain gene resistance selection, at 37°C in 5% CO<sub>2</sub>. Rat pheochromocytoma PC12  
147 cells (American Type Culture Collection; CRL 1721) were routinely grown in Dulbecco's  
148 Modified Eagle's Medium (DMEM, Gibco, Thermo Fisher Scientific) supplemented with 5%  
149 FBS, 10% sterile-filtered HyClone Donor Equine serum (GE Healthcare, Life Sciences), 100  
150 U ml<sup>-1</sup> penicillin, 100 µg ml<sup>-1</sup> streptomycin (Gibco, Thermo Fisher Scientific) and 1% L-  
151 glutamine 100X (Gibco, Thermo Fisher Scientific), at 37°C in 5% CO<sub>2</sub>. For  
152 immunofluorescence (IF) experiments, COS7-WT, PC12 and AtT20 cells were transfected  
153 with 0.8 µg of DNA encoding GFP-tagged human CgA (CgA-GFP), GFP-tagged human  
154 ΔPABD CgA (CgAΔPABD-GFP), GFP-tagged rat PDE4A1(PABD) (PDE4A1 WT) or GFP-  
155 tagged rat PDE4A1(mutated PABD) (PDE4A1 Mut), and 2 µl Lipofectamine 2000  
156 (Invitrogen) per well (24-well plate) according to the manufacturer's protocol. Four or five  
157 hours after the beginning of transfection, the culture medium was replaced by supplemented  
158 DMEM, and cells were additionally cultured for 24–48 h. For Western blot experiments,  
159 COS7-WT and AtT20 cells were transfected with 4 µg of DNA encoding CgA-GFP or  
160 CgAΔPABD-GFP, and 8 µl Lipofectamine 2000 (Invitrogen) per well (6-well plate)  
161 according to the manufacturer's protocol. Four or five hours after the beginning of  
162 transfection, the culture medium was replaced by supplemented DMEM, and cells were  
163 additionally cultured for 48 h.

164

### 165 **Plasmid constructs**

166 Full-length CgA-GFP (pCgA-EGFP-N2) kindly provided by M. Courel (UPMC, Paris,  
167 France) was used to amplify the sequence of CgA-encoding region by PCR using the sense  
168 primer (5'-CTCGAGGCCACCATGCGCTCCGCCGCTGTCTCGGCTTCTT-3'), including  
169 an XhoI restriction site (underlined bases), and the antisense primer (5'-

170 CCGCGGGCGCCCCGCCGTAGTGCCTGCA-3'), including a SacII restriction site before  
171 cloning into a pGEM-T vector (Promega, Charbonnières, France). Site-directed mutagenesis  
172 was conducted by using the QuickChange® II XL Site-Directed Mutagenesis Kit (Agilent  
173 technologies, Les Ulis, France) and specific primers (sense: 5'-  
174 CTCTCCTTCCGGGCCCCGGGCCTACGAGGACAGCCTTGAGGGCGGGCCTG-3';  
175 antisense: (5'-CAGGCCCGCCTCAAGGCTGTCCTCGTAGGCCCGGGCCCCGGAAGGAG  
176 AG-3') designed to remove the CgA PABD sequence (residues 364–381). The amplified  
177 mutated CgA (with deleted PABD region) was digested with the appropriate enzymes (XhoI  
178 and SacII) and subcloned into the eukaryotic expression vector pEGFP-N2. All the constructs  
179 were verified by restriction enzyme digestion and DNA sequencing. PDE4A1 WT and  
180 PDE4A1 Mut constructs were described previously (21).

181

## 182 **Animals**

183 *Pldl* knockout mice were described previously (22, 23). They were housed and raised at  
184 Chronobiotron UMS 3415. All experiments were carried out in accordance with the European  
185 Communities Council Directive of 24th November 1986 (86/609/EEC) and resulting French  
186 regulations. Accordingly, the CREMEAS local ethical committee approved all experimental  
187 protocols. Every effort was made to minimize the number of animals used and their suffering.

188

## 189 **Proteins and antibodies**

190 Recombinant CgA (human chromogranin A 19-457aa, His tag, *E. coli*, ATGP0323, Atgen  
191 global) was used for lipid strips and GUVs experiments. For CgA-Alexa488 coupling, all  
192 reactants and solvents were purchased from TCI-Chemicals and Alfa Aesar. CgA labeling  
193 was performed according to a modified version of a protocol reported in Chevalier et al. (24).  
194 First, 82 µl (1 eq.) of Alexa488 solution (2 mg ml<sup>-1</sup> in anhydrous N, N dimethylformamide)  
195 were introduced into a 1 ml round-bottom flask. (O-(N-succinimidyl)-N,N,N',N'-  
196 tetramethyluronium tetrafluoroborate (70 µg, 1.2 eq.) and N,N-diisopropylethyl-amine (0.04  
197 ml, 1.2 eq.) were added and the reaction medium was placed under argon, with magnetic  
198 stirring at RT during 1 h, to obtain the N-hydroxysuccinimidyl activated ester. A solution of  
199 250 µg of CgA in PBS buffer (pH 7.2, 0.5 mg ml<sup>-1</sup>, 1 eq.) was then slowly added dropwise in  
200 the reaction medium, for a ratio Alexa488/CgA 10/1. Reaction was carried out under argon,  
201 magnetic stirring and at RT overnight. Purification was performed using 10 kDa  
202 centrifugation filters (Spin-X® UF 500, CORNING) previously conditioned with PBS to

203 remove glycerol and other biocidal compounds. Labeled protein was collected in PBS buffer  
204 following 3 centrifugations of 10 min at 7,500 rpm. Grafting rate was evaluated by Western  
205 blot and UV-Vis spectroscopy ( $\lambda_{\text{abs}} = 494 \text{ nm}$ ), with a maximum labeling rate of 5.6  
206 Alexa488 molecules per protein.

207 Primary antibodies used were goat polyclonal anti-CgA (sc-23556; Santa-Cruz  
208 Biotechnology inc.) (1:200), rabbit polyclonal anti-CgA (WE-14 (25)) (1:1,000), rabbit  
209 polyclonal anti-CgA (RV31.4 (14) (1:1,000), rabbit polyclonal anti-SgII (EM66 (26))  
210 (1:1,000), goat polyclonal anti-CgB (sc-1489; Santa-Cruz Biotechnology inc.) (1:1,000),  
211 mouse monoclonal anti-GM130 (BDBiosciences) (1:1,000), mouse monoclonal anti-CALR  
212 (clone 1G11-1A9, Sigma-Aldrich) (1:1,000), mouse monoclonal anti-GLUD1 (clone 3C2,  
213 Sigma-Aldrich) (1:500), mouse monoclonal anti-golgin 97 (A21270; Invitrogen) (1:500),  
214 mouse monoclonal anti- $\alpha$ -tubulin (T5168, Sigma-Aldrich) (1:5,000). For IF, secondary  
215 antibodies used were Alexa 488-conjugated donkey anti-rabbit IgG; Alexa 594-conjugated  
216 donkey anti-mouse IgG (Invitrogen) (1:500). For Western blotting, anti-rabbit, anti-mouse  
217 and anti-goat secondary antibodies conjugated to horseradish peroxidase (Thermo Fisher  
218 Scientific) (1:5,000) were used.

219

### 220 **Protein-lipid binding assay**

221 Membrane lipid strips (P-6002, Echelon Biosciences) were saturated in PBS-T buffer (0.1%  
222 v/v Tween 20 in PBS) supplemented with 3% fatty acid-free BSA (Sigma-Aldrich) for 1 h at  
223 RT, and then incubated with  $500 \text{ ng ml}^{-1}$  recombinant human purified CgA diluted in this  
224 buffer for an additional hour at RT. After several washes with PBS-T, the membranes were  
225 incubated with anti-WE-14 antibody (1:1,000) 1 h at RT in the saturation buffer. After  
226 washing with PBS-T, membranes were incubated with a secondary antibody coupled to  
227 horseradish peroxidase (Thermo Fisher Scientific) and visualized by enhanced  
228 chemiluminescence. Densitometric analysis was performed to determine the relative affinity  
229 of CgA binding to various phospholipids.

230

### 231 **Subcellular fractionation**

232 Cells were collected in PBS and sedimented by centrifugation at  $400 g$  for 5 min at  $4^\circ\text{C}$ . The  
233 cell pellet was disrupted by 5 pulls/pushes through a 21- and then a 25-gauge needle attached

234 to a syringe, in ice-cold buffer (0.32 M sucrose, 20 mM Tris-HCl, pH 8; 1 ml g<sup>-1</sup> of cells). The  
235 resulting lysate was centrifuged at 800 g for 30 min at 4°C.

236

237 *Golgi membrane purification*

238 The protocol used was adapted from that developed by Graham et al (27) for the isolation of  
239 Golgi membranes from cultured cells by flotation through a discontinuous sucrose gradient.  
240 Briefly, Golgi membranes are isolated from low-speed pellets traditionally referred to as the  
241 nuclear pellet; hence the upper layer of the pellets (containing plasma, ER and Golgi  
242 membranes) were suspended in 1.4 M sucrose. The homogenate was deposited on a  
243 succession of 2 ml 1.4 and 2.0 M sucrose cushions and then covered with 2 ml 1.2 and 0.8 M  
244 sucrose cushions and 10 ml 0.32 M sucrose cushion, all sucrose cushions containing 10 mM  
245 Tris-HCl at pH 7.4. The extracts were then centrifuged at 10,000 g for 18 h at 4°C. The  
246 different fractions were collected in hemolysis tubes and kept at -20°C. An aliquot of each  
247 fraction was used for the localization of Golgi apparatus by Western blot using specific  
248 antibodies to recognize plasma membrane, Golgi, nucleus, mitochondria and the endoplasmic  
249 reticulum.

250

251 *Secretory granule purification*

252 Post-nuclear supernatants were centrifuged at 20,000 g for 20 min at 4°C. Pellets containing  
253 dense core granules were centrifuged on a multi-step gradient of 1 to 2.2 M sucrose (1, 1.2,  
254 1.4, 1.6, 1.8, 2 and 2.2 M sucrose; 5 ml steps), at 100,000 g for 12 h at 4°C. All gradient steps  
255 were collected from the top of the tube in 5 ml fractions, and analyzed by western blotting to  
256 identify the granule-containing fractions and to verify their degree of purification.

257

258 **Lipidomic analysis**

259 Total lipids from recovered Golgi and granule fractions were extracted by the method of  
260 Bligh and Dyer (28). Lipid extracts were resuspended in 50 µl of eluent A. Liquid  
261 chromatography coupled to tandem mass spectrometry (LC-MS/MS) analyses were  
262 performed with a MS model QTRAP® 6500 (Sciex) coupled to an LC system (1290 Infinity  
263 II, Agilent). Analyses were achieved in the negative (PA); nitrogen was used for the curtain  
264 gas (set to 15), gas 1 (set to 20) and gas 2 (set to 0). Needle voltage was at -4,500 without  
265 needle heating; the declustering potential was adjusted set at -180 V. The collision gas was  
266 also nitrogen; collision energy is set to -50eV. Reversed phase separations were carried out  
267 at 50°C on a Luna C8 150×1 mm column, with 100 Å pore size, 5 µm particles (Phenomenex,  
268 Torrance, USA). Eluent A was isopropanol/CH<sub>3</sub>OH/H<sub>2</sub>O+0.2 % formic acid+0.028 % NH<sub>3</sub>

269 and eluent B was isopropanol+0.2 % formic acid+0.028 % NH<sub>3</sub>. The gradient elution program  
270 was as follows: 0-5 min, 30-50 % B; 5 - 30 min, 50-80 % B; 31–41 min, 95 % B; 42–52 min,  
271 30 % B. The flow rate was set at 40 µl min<sup>-1</sup>; 3 µl sample volumes were injected. Quantitative  
272 PA analyses were made based on MS/MS multiple reaction monitoring (MRM) as described  
273 (29). Briefly, MRM transitions for individual PAs were determined using PA standards  
274 (Avanti Polar Lipids, Alabaster, USA). The predominant daughter fragment ions were then  
275 used for quantitative MRM analysis. MRM transitions and specific retention times were used  
276 to selectively monitor PA using MultiQuant software (v3.0, Sciex).

277

## 278 **Liposome and giant unilamellar vesicle formation and use**

### 279 *Liposome flotation and binding assays*

280 Lipids solubilized in chloroform were purchased from Avanti Polar Lipids (Alabaster, USA)  
281 and were used without further purification. Liposome mixtures were prepared in mass ratios  
282 composed of 90% DOPC (1,2-dioleoyl-*sn*-glycero-3-phosphocholine), 5% PE-NBD (1,2-  
283 dioleoyl-*sn*-glycero-3-phosphoethanolamine-N-(7-nitro-2-1,3-benzoxadiazol-4-yl)), and 5%  
284 PS (1,2-dioleoyl-*sn*-glycero-3-phospho-L-serine), PI(4,5)P<sub>2</sub> (1,2-dioleoyl-*sn*-glycero-3-  
285 phospho-(1'-myo-inositol-4',5'-bisphosphate)), egg PA mix or PA species (36:1 (1-stearoyl-2-  
286 oleoyl-*sn*-glycero-3-phosphate), 36:2 (1-stearoyl-2-linoleoyl-*sn*-glycero-3-phosphate), 40:6  
287 (1-stearoyl-2-docosahexaenoyl-*sn*-glycero-3-phosphate) or 36:0 (1,2-distearoyl-*sn*-glycero-3-  
288 phosphate). Lipids were dried in a stream of nitrogen and kept under vacuum for at least 2 h.  
289 Dried lipids were then suspended in liposome-binding buffer (LBB: 20 mM HEPES, pH 7.4,  
290 150 mM NaCl, 1 mM MgCl<sub>2</sub>) by three freeze and thaw cycles and were extruded using a  
291 Mini-Extruder (Avanti Polar Lipids, Alabaster, USA) through polycarbonate track-etched  
292 membrane filters to produce liposomes of 200 nm in diameter. The liposomes were then  
293 diluted in LBB (1:10) and incubated with 30 µg of COS7-CgA extract during 20 min. Then,  
294 samples were centrifuged at 200,000 g (1 h at 4°C) on a multi-step gradient sucrose. To  
295 determine the association of CgA with liposomes, the fractions were collected after  
296 centrifugation, and the presence of CgA was revealed using western blot analysis of the  
297 different fractions.

298 To quantify liposome binding to GST-CgA-PABD linked to GSH-Sepharose beads, GST and  
299 GST-PABD constructs (330 pmol) bound to GSH beads were washed once with 1 ml of LBB  
300 medium before incubation for 20 min in the dark at room temperature and under agitation  
301 with liposomes containing a 10-fold molar excess of PA relative to the quantity of GST

302 proteins in a final volume of 200  $\mu$ l of LBB. Beads were washed three times with 1 ml of ice-  
303 cold LBB and collected by centrifugation at 3,000 rpm for 5 min. Liposome binding to the  
304 PABD was estimated by measuring the fluorescence at 535 nm with a Mithras fluorimeter  
305 (Berthold). Triplicate measurements were performed for each condition. Fluorescence  
306 measured with GST linked to GSH-Sepharose beads alone was between 3 and 4 A.U. and was  
307 subtracted from sample measurements.

308

### 309 *Giant unilamellar vesicle preparation*

310 Giant unilamellar vesicles (GUVs) were prepared by polyvinyl acetate (PVA, MW 145000,  
311 purchased from VWR International, Fontenay-sous-Bois, France) – assisted swelling. Briefly,  
312 a Teflon plate was used and was cleaned twice with 99% ethanol. A 5% (w/w) solution of  
313 PVA was prepared by stirring PVA in water while heating at 90°C. PVA-coated substrates  
314 were prepared by spreading 100–300  $\mu$ l of PVA solution on a clean Teflon plate, and dried  
315 for 30 min at 80°C. 10–20  $\mu$ l of a lipid mixture (95% of DOPC, 4% of PA (36:1) or (40:6)  
316 and 1% of PE-NBD) dissolved in chloroform (1 mg ml<sup>-1</sup>) was spread on the dried PVA film  
317 and placed under vacuum overnight at RT to evaporate the solvent. A chamber around the  
318 drops of lipids was formed with Vitrex and filled with 100 mM sucrose and 150 mM NaCl  
319 solution during 3 h at room temperature, allowing the formation of GUVs with a suitable size.  
320 Next, the buffer containing GUVs is recovered using a rib with a wide tip to avoid destroying  
321 the GUVs, and deposited in LabTek wells (LabTek I non-separable, on glass coverslip, 4  
322 culture chambers, Nunc), which were previously coated with a 1 mg ml<sup>-1</sup> BSA (Bovine Serum  
323 Albumin, Sigma – Aldrich) solution. To allow the sedimentation of GUVs, we added the  
324 same volume (100  $\mu$ l) of a solution containing 90 mM glucose and 15 mM NaCl in LabTek  
325 wells. The sedimentation of the GUVs takes place for about 1 h at RT.

326 To test the effect of CgA on the GUV membranes, we added CgA or CgA-Alexa488 in GUV-  
327 containing Labtek wells at a final concentration of 2, 4 or 6  $\mu$ M just before the beginning of  
328 confocal microscopy acquisitions.

329

### 330 *Small unilamellar vesicle preparation*

331 Small unilamellar vesicles (SUVs) were prepared using the standard extrusion method as  
332 described previously for liposome formation. Liposome mixtures prepared in mass ratios  
333 composed of 90% DOPC, 10% PA (36:1) were dissolved in a test tube with chloroform.  
334 Lipids were dried under argon gaz. The lipid film thus obtained was hydrated with 500  $\mu$ l of

335 water and the solution was subjected to vortex mixing for 1 h at room temperature. The  
336 multilamellar vesicles were extruded 27 times using the Mini-Extruder equipped with a  
337 polycarbonate membrane filter of 100 nm pore diameter to obtain SUVs.

338

### 339 **Atomic force microscopy measurements**

#### 340 *Membrane preparation*

341 Giant Unilamellar Vesicles (GUVs) were prepared by using 100% DOPC or a mix of 90%  
342 DOPC and 10% PA (36:1). The vesicles were prepared in a 200 mM sucrose solution. GUV  
343 solution was diluted 100 times in 250 mM glucose solution to promote their sedimentation  
344 and to avoid multilayers. Final lipid concentration was 10  $\mu\text{M}$ . The vesicle solution was  
345 injected in the AFM liquid cell and put in contact with freshly cleaved mica. After 2 min, the  
346 vesicle solution is replaced with 250 mM glucose solution in order to maintain the supported  
347 lipid bilayers hydrated at all times during imaging. To study protein/lipid interactions, the  
348 glucose solution was replaced with a CgA solution (0.6 or 1.2  $\mu\text{M}$ ), and the sample was  
349 imaged again.

350

#### 351 *Microscopy imaging*

352 AFM measurements were performed on a multimode atomic force microscope (Nanoscope  
353 IIIA, Veeco, USA). Supported lipid bilayers images were taken in tapping mode in the fluid  
354 cell. A soft cantilever with a typical spring constant of 0.06 N/m and equipped with a silicon  
355 nitride tip was used. The tip velocity was set between 5-10  $\mu\text{m/s}$  by varying the scan rate  
356 according to the scan size. The cantilever oscillation was tuned to a frequency between 20 and  
357 30 kHz, and the amplitude was set between 0.8 V and 2 V. All the experiments were carried  
358 out at a temperature of 21°C.

359

### 360 **High-sensitivity isothermal titration calorimetry**

361 Isothermal titration calorimetry (ITC) was performed on an Affinity instrument (TA  
362 Instrument, New Castle, DE) equipped with a 185  $\mu\text{l}$  reaction chamber. Solutions were  
363 degassed under low pressure before use to avoid the formation of air bubbles while titrating.  
364 The CgA solution (5  $\mu\text{M}$ ) was placed in the calorimeter chamber and SUV suspension (10  
365 mM) was injected in aliquots of 2.5  $\mu\text{l}$ . The period between two successive injections was  
366 typically 200 sec to allow the system to reach equilibrium. The solution was stirred

367 continuously at 125 rpm and the experiments were carried out at a temperature of 10°C. The  
368 resulting heat changes after SUV injection were recorded as a function of time. The heat of  
369 reaction was obtained by integrating the area under each peak of heat flow tracings, using the  
370 heat of SUV dilution in water as blank sample. The data were acquired by using the  
371 Nanoanalyze software (v.3.10.0, TA Instrument).

372

### 373 **Immunofluorescence labelling**

374 COS7-CgA cells were cultured in 24-well plates (Costar® 24 Well Clear TC-Treated  
375 Multiple Well Plates, Corning), onto glass coverslips and fixed with 4% paraformaldehyde  
376 (Sigma – Aldrich) in PBS at RT for 15 min. Cells were permeabilized and blocked for 30 min  
377 with 0.3% Triton X-100 (Thermo Fisher Scientific), in PBS containing 5% normal donkey  
378 serum (Sigma – Aldrich) (1:50) and 1% BSA. Cells were then incubated for 2 h at RT with  
379 primary antibodies, and, after washing with PBS, for 1 h with secondary antibodies. Nuclei  
380 were stained with DAPI (4',6-diamidino-2-phenylindole, Molecular probes) (1 µg ml<sup>-1</sup>). To  
381 verify the specificity of the immunoreactions, the primary or secondary antibodies were  
382 substituted with PBS.

383

### 384 **Protein electrophoresis and Western blotting**

385 Cells were harvested by scraping in NP40 cell lysate buffer (Thermo Fisher Scientific)  
386 supplemented with a cocktail of protease inhibitors (Thermo Fisher Scientific), homogenized,  
387 and proteins were separated by SDS-PAGE followed by Western blotting. Membranes were  
388 incubated in a blocking buffer containing 5% non-fat dry milk in PBS containing 0.5% Tween  
389 20 (Sigma - Aldrich) (PBS-T) for 1 h at RT, and overnight with primary antibodies at 4°C.  
390 Then, membranes were washed for 45 min with PBS-T. Blots were subsequently incubated  
391 for 1 h with appropriate HRP (Horse Radish Peroxidase)-conjugated secondary antibody  
392 (Thermo Fisher Scientific) in blocking buffer. Membranes were washed for 45 min with PBS-  
393 T and immunoreactive proteins were detected by chemiluminescence (BioRad  
394 Biotechnology). Quantification was performed using Image Lab software (5.0 build 18, 2013  
395 version, Bio-Rad Laboratories). The mean intensity of each individual band of interest was  
396 calculated after background value subtraction.

397

### 398 **Image acquisition**

399 For GUVs experiments, real-time videomicroscopy was carried out with an inverse confocal  
400 microscope TCS-SP5 AOBS (*Acousto-Optical Beam Splitter*), equipped with pulsed white  
401 light laser (WLL) and with a 63X oil immersion objective (Leica Microsystems). PE-NBD  
402 was excited at 463 nm and observed in a 510-550 nm window. Images were acquired at a  
403 speed of one frame per 2 s during 1 min.

404 For immunocytochemistry experiments, confocal microscopy was carried out with a TCS-SP8  
405 upright confocal laser-scanning microscope equipped with 63X oil immersion objective  
406 (NA=1.4; Leica, Microsystems). Alexa 488 and GFP were excited at 488 nm and observed in  
407 a 505–540 nm window. Alexa 594 was excited at 594 nm and observed in a 600–630nm  
408 window. For dual color acquisition, images were sequentially acquired in line scan mode  
409 (average line = 2). Overlays were performed with post acquisition Leica Confocal Software  
410 functions to obtain the presented snapshots.

411 For super-resolution experiments, image acquisitions were performed with a 100X oil  
412 immersion objective (NA 1.4) through time-gated continuous wave stimulated emission  
413 depletion (gCW STED) imaging (TCS SP5-X; Leica Microsystems) (30) with optimized  
414 parameters for GFP detection (Supplemental Fig. 2). Samples (zoom 8, pixel size = 18.95 nm)  
415 were excited with a 488 nm wavelength of a supercontinuum laser (20–30% AOTF). A  
416 conventional scanner (400 Hz, Line Average 1, Frame Average 1, Frame Accumulation 3,  
417 1024 × 1024) was used. Depletion was obtained with a 592 nm laser (70% AOTF).  
418 Fluorescence (500–550 nm) was collected with a hybrid detector (Gain 100) in the gated  
419 mode and a pinhole for Airy 1.

420

#### 421 **Transmission electron microscopy of WT and *Pld1*<sup>-/-</sup> chromaffin cells in situ**

422 WT and *Pld1*<sup>-/-</sup> mice were anesthetized with a mixture of ketamine (100 mg kg<sup>-1</sup>) and xylazine  
423 (5 mg kg<sup>-1</sup>) and transcardially perfused with 0.1 M phosphate buffer, pH 7.3, containing 2%  
424 paraformaldehyde and 2.5% glutaraldehyde. The 2-mm-thick slices were cut from the adrenal  
425 glands and postfixed in 1% glutaraldehyde in phosphate buffer overnight at 4°C. The slices  
426 were then immersed for 1 h in OsO<sub>4</sub> 0.5% in phosphate buffer. 1-mm<sup>3</sup> blocks were cut in the  
427 adrenal medulla, dehydrated, and processed classically for embedding in Araldite and  
428 ultramicrotomy. Ultrathin sections were counterstained with uranyl acetate and examined with  
429 a Hitachi 7500 transmission electron microscope.

430

#### 431 **Post-acquisition analysis**

432 The following procedure was used to measure the number of CgA granules. The confocal  
433 section generated by the Leica TCS-SP8 confocal microscope was analyzed with Imaris and  
434 converted into an Imaris file. A broad region of interest (ROI) was defined around a cell.  
435 Then with the tool 'spots detection' on Imaris, the number of spots with a diameter > 200 nm  
436 was quantified. Spots statistics are automatically computed for each spot object. It provides a  
437 procedure to automatically detect point-like structures, an editor to manually correct detection  
438 errors, a viewer to visualize the point-like structures as spheres, and statistics output.

439 To analyze secretory granule density in wild-type (WT) and *Pld1* knock-out chromaffin cells,  
440 secretory granules were counted in 50 chromaffin cells from WT and *Pld1* KO mice with a  
441 visible nucleus randomly selected in ultrathin sections from several blocks (1 section/block)  
442 from each mouse (n=3 mice per genotype). Dense core diameter was measured from 950  
443 randomly selected granules for each genotype using the line segment tool of Image J. To  
444 minimize the bias measurements, samples were blinded.

445 To improve signal-to-noise ratio in STED images, deconvolution of raw data was obtained  
446 through image processing with Huygens professional 4.5.1 software (SVI, The Netherlands)  
447 (31).

448

#### 449 **Statistics**

450 Data were analyzed with the Prism program (GraphPad 6.04 Software). For the quantification  
451 of the number of CgA granules in IF studies, statistical significance was determined by Mann-  
452 Whitney U test. Values are expressed as means  $\pm$  s.e.m. or S.D., and the level of significance  
453 is designated in the figure legend as follows: \*  $P < 0.05$ , \*\*  $P < 0.01$ , \*\*\*  $P < 0.001$ . For the  
454 quantification of CgA signal in lipid strip experiments, statistical significance was determined  
455 by an Anova one-way analysis of variance test with Bonferroni's comparison test. Values are  
456 expressed as means  $\pm$  s.e.m., and the level of significance is designated in the figure legend as  
457 follows: \*\*\*  $P < 0.001$ . For the quantification of membrane deformation after CgA addition on  
458 GUVs, statistical significance was determined by Mann-Whitney U test. Values are expressed  
459 as means  $\pm$  s.e.m., and the level of significance is designated in the figure legend as follows:  
460 \*\*\*  $P < 0.001$ . For the quantification of the number of secretory granules and their dense core  
461 diameter in MET study, statistical significance was determined by Mann-Whitney U test.  
462 Values are expressed as means  $\pm$  s.e.m., and the level of significance is designated in the  
463 figure legend as follows: \*  $P < 0.05$ .

464



## 466 **RESULTS**

### 467 **Chromogranin A interacts preferentially with PA**

468 Due to the presence of two helicoidal motives in its N- and C-terminal conserved regions  
469 which bear the granulogenic activity of CgA and which can promote binding to lipids (11),  
470 we analyzed the capacity of the granin to interact with membrane lipids. A lipid overlay assay  
471 was performed by incubating recombinant CgA with a nitrocellulose sheet where different  
472 membrane lipids were adsorbed. Using an antibody raised against CgA (25), this overlay  
473 assay revealed that CgA interacts with PA and phosphoinositides (PIP, PIP<sub>2</sub> and PIP<sub>3</sub>) (Fig. 1  
474 A). Quantification of the CgA-lipid interaction signals revealed that CgA preferentially  
475 interacts with PA (Fig. 1 A).

476

### 477 **Golgi PA is involved in the biogenesis of CgA-containing secretory granules**

478 To examine the importance of PA in the formation of CgA-induced secretory granules, we  
479 overexpressed the PABD of the cytosolic phosphodiesterase PDE4A1 in neuroendocrine  
480 PC12 cells in order to reduce the ability of CgA to interact with PA in Golgi membranes.  
481 Indeed, PDE4A1 PABD was previously shown to interact with PA specifically at the TGN in  
482 COS1 cells (32) and RAW264.7 macrophages (21), and its overexpression should reduce the  
483 amount of available PA at this level. We found that PDE4A1(PABD) not only exhibited the  
484 expected Golgi-like confined localization, but also significantly reduced the number of CgA  
485 secretory granules, without affecting CgA expression (Fig. 1 B). Moreover, expression of  
486 PDE4A1(PABD Mut) which does not bind to PA and which was not detected in the Golgi  
487 area did not impair the biogenesis of CgA-induced granules (Fig. 1 B), strongly supporting  
488 the crucial role of Golgi PA in the formation of CgA secretory granules.

489

### 490 **Chromogranin A interacts with PA through a putative PA-binding domain**

491 To characterize the CgA region involved in PA binding, we compared the CgA helicoidal  
492 motifs with those of proteins with known PABD, notably the Golgi PA-binding protein  
493 PDE4A1. This analysis revealed a potential PABD within residues 352-381 of CgA, a  
494 sequence containing positively charged and hydrophobic amino acids (Fig. 1 C). Indeed, a  
495 bioinformatics analysis using Heliquest software (33) further refined this PABD to residues  
496 364 - 381 (Fig. 1 C), which shares the characteristics of typical PABDs (34). It is predicted  
497 that this PABD adopts an amphipathic  $\alpha$ -helical conformation with five positively charged

498 residues (arginines) sequestered in one side of the helix, which could interact with the  
499 negatively charged polar head of PA, and three surface exposed hydrophobic residues  
500 (tryptophane, phenylalanine, leucine) on the other side of the helix which could insert within  
501 the hydrophobic part of membranes and interact with the fatty acid chains of PA (Fig. 1 D).  
502 Interestingly, a 3D structural model of CgA PABD confirmed that this domain displays an  $\alpha$ -  
503 helix when its structure was examined using MacPyMol software (shown as a ribbon, Fig. 1  
504 E). We then used a semi-quantitative *in vitro* assay with NBD-labeled liposomes (21) to  
505 investigate the PA binding capacity of three different GST fusion proteins containing the C-  
506 terminal helicoidal motif of CgA or parts of it: CgA(352-381) (CgA PABD), CgA(352-372)  
507 (catestatin) and CgA(373-381). We found that GST-CgA(352-381) very efficiently bound  
508 PA-containing liposomes, while the binding of GST-CgA(352-372) was greatly reduced and  
509 that of GST-CgA(373-381) was even lower (Fig. 1 F). In contrast, none of the proteins tested  
510 efficiently bound PC NBD-liposomes (Fig. 1F), highlighting the preferential affinity of the  
511 CgA  $\alpha$ -helix for PA rather than for curved membranes. These data not only indicate that the  
512 entire sequence corresponding to CgA PABD is important for PA binding but also that CgA  
513 proteolysis, as it occurs in secretory granules and which generates the peptide catestatin  
514 (CgA(352-372)) (Fig. 1 C), should disrupt this binding.

515

### 516 **Specific PA species are predominant and common to Golgi and secretory granule** 517 **membranes from CgA-expressing cells**

518 We analyzed and compared the PA content of Golgi and secretory granule membrane  
519 fractions purified from COS7 cells stably expressing CgA (COS7-CgA). These cells display  
520 CgA-containing secretory granule-like structures in contrast to their WT counterparts with no  
521 CgA (14, 15). The enrichment of secretory granule and Golgi membrane fractions was  
522 evaluated by western blotting (Supplemental Fig. 1). Detailed lipidomics analysis of these  
523 fractions revealed that over the 44 distinct species detected, only few specific PA species are  
524 predominantly identified in secretory granule and Golgi membranes of COS7-CgA cells, *i.e.*  
525 PA (36:1), PA (38:2), PA (38:6) and PA (40:6) (Fig. 2 A). Furthermore, we compared the  
526 Golgi membrane of COS7-WT and COS7-CgA cells to examine the potential impact of CgA  
527 expression on the PA content. We found that the Golgi membrane of COS7-WT and COS7-  
528 CgA cells exhibit the same predominant PA species, *i.e.* PA (36:1), PA (38:2) and PA (40:6),  
529 but we also noticed a significant enrichment in PA (36:1) in Golgi membranes after CgA  
530 expression, mainly at the expense of PA (40:6) (Fig. 2 B). The presence of the same major PA

531 species, namely PA (36:1), PA (38:2) and PA (40:6), was also found in secretory granule  
532 membranes isolated from the neuroendocrine PC12 cells (Fig. 2 C). These data suggest that  
533 PA (36:1), PA (38:2) and PA (40:6) could represent crucial species for secretory granule  
534 formation.

535

### 536 **Chromogranin A interacts with major Golgi/secretory granule PA species included in** 537 **giant liposomes and induces membrane deformation and vesicle budding**

538 To test the interaction between CgA from COS7-CgA cell extracts and the predominant PA  
539 species identified in Golgi and secretory granule membranes, we used a liposome flotation  
540 assay (Fig. 3 A). Following the flotation assay, the different fractions were analyzed by  
541 western blotting using a CgA specific antibody (25). This analysis revealed a strong  
542 interaction between CgA and liposomes enriched with PA species identified previously by  
543 lipidomics analysis, with an apparent preference for PA (36:1), and far less interaction with  
544 PIP<sub>2</sub>-enriched liposomes (Fig. 3 B). In contrast, no interaction was found with liposomes  
545 enriched with phosphatidylcholine (PC), phosphatidylserine (PS) or PA (36:0), in accordance  
546 with the results obtained using lipid strips (Fig. 1 B; Fig. 3 B). These results demonstrate that  
547 endogenous CgA interacts specifically with predominant PA species identified in Golgi and  
548 secretory granule membranes from CgA-expressing cells.

549 To examine the membrane dynamics following CgA and PA interaction, we developed  
550 a model of GUVs enriched in PA (36:1) or PA (40:6), whose formation is assisted by a  
551 polyvinyl alcohol gel. To analyze their morphology using confocal microscopy, we generated  
552 PA-enriched GUVs containing a fluorescent lipid, phosphatidylethanolamine (PE)-NBD.  
553 After image acquisitions, we observed that the formed GUVs exhibit a diameter ranging  
554 between 5 and 50  $\mu\text{m}$ , that the fluorescence is homogeneously distributed around the GUVs  
555 and that there are no budding events (Fig. 3 C; supplemental video 1). Addition of 2  $\mu\text{M}$  CgA  
556 to PA-enriched GUVs provoked a marked fluorescence concentration in confined membrane  
557 domains of several GUVs just before budding events which resulted in the formation of small  
558 vesicles (Fig. 3 D; supplemental video 2). Quantification of membrane deformations  
559 generating vesicles revealed that the number of budding events depends on CgA  
560 concentration (Fig. 3 E). Finally, to analyze the direct involvement of CgA in GUV  
561 membrane remodeling, we generated a CgA fluorescent probe, CgA-Alexa488, and we  
562 observed that addition of 2  $\mu\text{M}$  CgA-Alexa488 on non-fluorescent PA-enriched GUVs results  
563 first in a rapid and homogenous fluorescence distribution in GUV membranes, and then

564 within a minute budding events were detected in fluorescent CgA-enriched membrane  
565 domains (Fig. 3 F). Altogether, these results indicate that CgA interacts with membrane PA  
566 and that this interaction could induce a membrane remodeling resulting in vesicle budding.

567

### 568 **Thermodynamic characteristics of CgA/PA interaction indicate that PA favors CgA** 569 **incorporation in liposome membranes**

570 To investigate the CgA/PA interaction in more details, we conducted an ITC analysis, which  
571 quantifies the binding equilibrium directly by measuring the heat change resulting from the  
572 association of a ligand with its binding partner (35, 36). ITC thermograms showed that  
573 injection of a water suspension of small unilamellar vesicles (SUVs) composed of 1,2-  
574 dioleoyl-sn-glycero-3-phosphocholine (DOPC) or DOPC/PA (36:1) induced an exothermic  
575 process resulting from the dilution process of SUVs in water (Fig. 4, A and B, upper panels).  
576 When we injected DOPC or DOPC/PA (36:1) SUV suspension into a CgA solution, the ITC  
577 results showed sequential exothermic and endothermic processes (Fig. 4, A and B, lower  
578 panels). Enthalpy curves (Fig. 4 C) were obtained from the integrated energy values obtained  
579 from A and B traces in lower panels, using A and B traces in upper panels as blank,  
580 respectively. These curves were fitted using two simple one-site binding model to yield  
581 thermodynamic parameters (Table 1). Comparing the enthalpy curves obtained after DOPC  
582 and DOPC/PA (36:1) injection in CgA solution, we observed an increase due to an  
583 exothermic process related to the binding of CgA with DOPC that could result from hydrogen  
584 bonding and/or electrostatic force (18). We also noticed that the maximum of enthalpy is  
585 reached after 14 injections of DOPC SUVs while it is reached only after 6 injections of  
586 DOPC/PA (36:1) SUVs (Fig. 4 C). In addition, for the exothermic process, the calculated  
587 enthalpy ratio  $\Delta H_{DOPC/PA(36:1)}^{exo}/\Delta H_{DOPC}^{exo}$  is close to 7, the enthalpy ratio  
588  $\Delta H_{DOPC/PA(36:1)}^{endo}/\Delta H_{DOPC}^{endo}$  is equal to 12, and the stoichiometry (n) for both processes is lower  
589 with DOPC/PA (36:1) SUVs (Table 1). Moreover, the endothermic phase leads to enthalpy  
590 decrease (Fig. 4 C) and the stoichiometric ratio, which is the ratio between the total number of  
591 lipids and the number of lipids on the outer surface of the SUV, is close to 1.8, suggesting a  
592 reorganization of the protein/lipid complex in the SUV membrane. Together, these results  
593 clearly show that PA favors the incorporation of CgA in the SUV membrane.

594

595

596 **Chromogranin A induces the remodeling of supported membrane bilayers enriched with**  
597 **Golgi/secretory granule PA**

598 Using atomic force microscopy (AFM), we studied the impact of CgA on supported bilayers  
599 composed of DOPC or DOPC/PA (36:1). Addition of 0.6 or 1.2  $\mu\text{M}$  CgA during 15 min (T1)  
600 and 75 min (T2) on DOPC membranes revealed small alterations of their topographical  
601 profile corresponding to protrusions with a maximal height of 4 nm (Fig. 5 A). In contrast,  
602 addition of 0.6 or 1.2  $\mu\text{M}$  CgA on DOPC/PA (36:1) membranes led to local profile changes of  
603 the membrane with a height of the protrusions above 4 and 16 nm, respectively (Fig. 5 B). Of  
604 note, the grain size analysis of 11-15 images obtained with 1.2  $\mu\text{M}$  CgA during 75 min  
605 revealed that the total number of CgA-induced domains increases by a factor of 3 after PA  
606 (36:1) addition in DOPC bilayers ( $41\pm 23$  domains per  $100 \mu\text{m}^2$  DOPC bilayer (Fig. 6 A)  
607 versus  $120\pm 41$  domains per  $100 \mu\text{m}^2$  DOPC/PA (36:1) bilayer (Fig. 6 B)). Moreover, domains  
608 with an area greater than  $20 \mu\text{m}^2$  were clearly more abundant in presence of PA (36:1) in the  
609 supported bilayer, and their height increased with their area to reach a mean of  $21\pm 3$  nm (Fig.  
610 6 B). These results suggest that CgA interacts with PA-enriched lipid bilayers and that this  
611 interaction modifies membrane topology, in a concentration and time-dependent manner.

612

613 **Chromogranin A PABD is required for secretory granule biogenesis**

614 To analyze the role of the predicted CgA PABD in the formation of secretory granules, we  
615 expressed CgA where the PABD was deleted (CgA $\Delta$ PABD-GFP) in COS7 and AtT20 cells.  
616 This specific CgA alteration significantly reduced secretory granule formation as compared to  
617 native CgA (Fig. 7, A and B). Indeed, although CgA $\Delta$ PABD-GFP and CgA-GFP both  
618 colocalized with the Golgi marker GM130, the number of CgA positive granules is reduced  
619 when the PABD is deleted from CgA in COS7 cells (Fig. 7 A), but also in ATt20 cells  
620 although transfection efficiency was lower (Fig.7 B). Using deconvoluted time-gated  
621 continuous wave stimulated emission depletion (gCW STED) nanoscopy to overcome the  
622 noise at the Golgi level (Supplemental Fig. 2), we confirmed a reduction of CgA-containing  
623 structures in the Golgi area of both cell types expressing CgA $\Delta$ PABD-GFP (Fig. 7, C and D).  
624 Altogether, these results support the idea that the interaction of CgA with PA through its  
625 PADB is important for granule biogenesis.

626

627

## 628 **Inhibition of PLD-mediated PA synthesis alters the biogenesis of secretory granules**

629 To study the implication of PA in Golgi membranes during the biogenesis of CgA-containing  
630 secretory granules, we altered PLD-mediated PA synthesis since PLD appears to be the most  
631 important provider of PA in the Golgi (37). First, secretory cells were incubated with the PLD  
632 pan-inhibitor FIPI, which provoked a significant reduction in the number of CgA-containing  
633 granules in COS7-CgA cells (Fig. 8 A) and a smaller reduction in PC12 cells (Fig. 8 B),  
634 without any apparent effect on the levels of three major granins (CgA, CgB, SgII).  
635 Interestingly, in chromaffin cells obtained from mice lacking *Pld1* gene (*Pld1*<sup>-/-</sup>), we observed  
636 by electron microscopy a significant reduction in the number of secretory granules (Fig. 8, C  
637 and D), associated to a decrease in their dense core diameter (Fig. 8, C and E). Thus,  
638 pharmacological and genetic invalidation of PLD activity and expression supported the notion  
639 that PLD1 is an important provider of PA in Golgi membranes (38), and showed that PLD1-  
640 generated PA is required for the biogenesis of secretory granules containing CgA.

641

## 642 **DISCUSSION**

643 Although considerable efforts have been deployed to identify the molecular mechanism at the  
644 origin of secretory granule formation, many aspects of this fundamental process remain to be  
645 elucidated. The biogenesis of secretory granules depends on TGN membrane dynamics that  
646 rely on interactions of cytosolic and luminal proteins with molecular components of the TGN  
647 membrane. Among TGN luminal proteins, members of the granin protein family have been  
648 long considered as major actors of secretory granule biogenesis but direct mechanistic  
649 evidence is still lacking (39).

650 Here, we first uncovered the ability of the coiled-coil glycoprotein CgA to bind acidic  
651 phospholipids, in particular PA, using a lipid-overlay assay. Since PA was suspected to play a  
652 role in secretory granule biogenesis (40), we overexpressed the cytosolic phosphodiesterase  
653 PDE4A1, a *bona fide* PA binding protein in Golgi membranes characterized previously (21)  
654 to test this possibility. We observed a decrease in the number of CgA-containing secretory  
655 granules in PC12 cells in the presence of PDE4A1-PABD, presumably acting as a competitor  
656 for endogenous PA, suggesting that luminal CgA requires TGN membrane PA to generate  
657 secretory granules. As most enzymes involved in PA synthesis are found in the cytoplasmic  
658 leaflet of intracellular membranes, it is expected that most PA is generated in these membrane  
659 cytosolic leaflets. However, passive PA flip/flop or active PA-transfer by flippase, floppase  
660 and scramblase could efficiently alter this translayer asymmetry for PA. Accordingly, we

661 observed that PA was readily detected on the inner leaflet of the plasma membrane of PC12  
662 cells expressing the PA binding protein Spo20p-GFP less than one minute after cell  
663 incubation with 10 $\mu$ M of PA micelles (unpublished observation). Additionally, *in vitro*  
664 experiments have suggested that intrinsic flipping of PA is affected by various parameters  
665 including pH and the geometry of specific PA species (41, 42). Thus, it is likely that  
666 significant levels of PA are present in the luminal leaflet of the TGN and therefore CgA/PA  
667 interaction could be effective at this location.

668 *In silico* identification of the CgA(364-381) sequence as a PABD further supported the  
669 possibility of CgA/PA interaction, which was confirmed using PA-enriched liposomes, as this  
670 sequence specifically binds PA. Interestingly, CgA PABD binds PA at a level similar to that  
671 observed for PDE4A1. In contrast, shorter fragments, corresponding to the expected cleavage  
672 of CgA occurring during secretory granule maturation to generate catestatin, exhibited only a  
673 weak interaction with PA. We can therefore anticipate that CgA/PA interaction might be  
674 regulated during secretory granule maturation and CgA processing. It is tempting to speculate  
675 that CgA and PA interact early in the TGN to trigger secretory granule formation, but that this  
676 interaction is disrupted later by proteolysis after budding to generate catestatin and to ensure  
677 secretory granule homeostasis. Such a sequential role has previously been demonstrated for  
678 the granin 7B2 in the regulation of the proteolytic enzyme PC2 and hormone sorting and  
679 secretion in endocrine cells (43). Moreover, the CgA PABD sequence may allow hydrophobic  
680 residue insertion into lipid bilayers and direct ionic interaction between basic residues and  
681 several PA molecules. Thus, CgA may participate to TGN remodeling by interacting with  
682 TGN predominant PA species that could induce the formation of PA-enriched microdomains.  
683 Indeed, CgA represents 40 to 80% of the protein content of secretory granules in chromaffin  
684 cells and the concentration is in the order of millimolar, representing around 5,000 CgA  
685 molecules per granule (44, 45). On the other hand, molecular dynamic simulation of the  
686 interaction of PA with the yeast protein Spo20p PABD revealed that up to 6 PA molecules  
687 bind to one Spo20p molecule (46). Based on the number of positively charged residues in the  
688 CgA PABD, it is possible that one CgA binds and sequesters up to 5 PA. Therefore, this can  
689 yield an extremely high density of PA, with up to 25,000 molecules accumulating with CgA  
690 on specific locations of the inner leaflet of the TGN membrane. Accumulation of the conical-  
691 shaped PA enables membrane bending (47), and this phenomenon could generate TGN  
692 membrane curvature preceding secretory granule budding.

693 To further support the role of PA in secretory granule formation, we analyzed and  
694 compared the PA composition in Golgi and secretory granule membranes from COS7-CgA  
695 cells by mass spectrometry, and found a strong similarity in the PA species present in the  
696 membranes of these two compartments. Among these PA species, we observed a  
697 predominance of several common mono- and poly-unsaturated forms, *i.e.* PA (36:1) and PA  
698 (40:6). Interestingly, these PA species were also identified in the membrane of secretory  
699 granules from neuroendocrine PC12 cells, suggesting that specific PA species occur at the  
700 Golgi membrane of CgA-expressing cells to induce the biogenesis of secretory granules, and  
701 that one or some of these species have a key role in this process. Using liposome models  
702 enriched with distinct phospholipids, we observed that CgA preferentially interacts with PA  
703 (36:1) and PA (40:6), and that addition of this granin generates deformation of PA (36:1)- or  
704 PA (40:6)-enriched artificial membranes in a dose-dependent manner. Of note, budding  
705 occurs in an outward direction from PA-enriched giant liposome membrane towards CgA,  
706 contrasting with the required budding towards the cytosol required for secretory granule  
707 formation. This apparent discrepancy is probably due to the fact that native membranes are  
708 more complex than artificial membranes in terms of lipid variety and asymmetric distribution  
709 between the two leaflets, in addition to the presence of other membrane proteins and the  
710 impact of cytosolic and luminal membrane environment (pH, ion concentration, cytosolic  
711 proteins). The hydrophobic face of CgA PABD helix was proposed to partially insert into  
712 artificial membrane, stressing nearby lipid packing, creating local defects, and promoting  
713 membrane curvature. In any case, the fact that generated buds stay attached to the GUV  
714 surface is consistent with the absence of cytosolic proteins involved in vesicle fission, such as  
715 dynamin. The analysis of the thermodynamic characteristics of CgA/PA (36:1) interaction by  
716 ITC consolidated the observation that CgA strongly interacts with PA (36:1)-enriched  
717 membranes to promote membrane deformation. Atomic force microscopy on supported  
718 membrane bilayers revealed that PA (36:1) enrichment increased the number, the height and  
719 the surface of CgA-induced domains resulting from either CgA aggregation, membrane  
720 deformation, microdomain formation, or any combination of these. These data support a  
721 central role for PA in the formation of CgA-induced domains as observed by confocal  
722 microscopy and ITC. Altogether, these results are in line with the idea that CgA/PA (36:1) or  
723 PA (40:6) interaction could play a key role in the membrane remodeling process necessary for  
724 secretory granule budding.

725 In accordance, we showed that expression of CgA deprived from its PABD leads to a  
726 significant decrease in the number of CgA granules, with a reduction of CgA granule number  
727 in whole cell but also in the Golgi area. The CgA-PABD deletion mutant is apparently acting  
728 as a negative-dominant impairing CgA-induced granule formation, probably by disrupting the  
729 molecular interactions normally occurring between CgA and PA at Golgi membranes.  
730 Therefore, these data support the notion that CgA-PABD is involved in granule biogenesis  
731 and that CgA/PA interaction through this domain is critical for the initiation of the secretory  
732 process in neuroendocrine cells. Interestingly, the C-terminal sequence of catestatin  
733 (CgA(352-372)) including the PABD contains several single nucleotide polymorphisms  
734 associated with metabolic and cardiovascular disorders in humans (48, 49), suggesting a  
735 potential link between the onset of these diseases and the disruption of hormone release  
736 related to an alteration of CgA secretory granule biogenesis.

737 Moreover, several studies demonstrated that the enzymatic activity of PLD1  
738 converting PC to PA is an important source of Golgi PA (38), which is required for secretory  
739 granule budding (50), but also involved in secretory granule fusion with the plasma  
740 membrane (51). Pharmacological inhibition of PLD in COS7-CgA and PC12 cells, and *Pld1*  
741 knockout in mouse chromaffin cells, both reduced secretory granule biogenesis. The smaller  
742 reduction in PC12 could be due to the endogenous expression of additional granin family  
743 members endowed with a granulogenic effect and which could act through PLD/PA-  
744 independent manner. Interestingly, this reduction in secretory granule number was also  
745 accompanied by an alteration in the shape of these organelles, very similarly to what was  
746 found in CgA-knockout chromaffin cells (52), indicating that PLD1 depletion partially  
747 phenocopies CgA deficiency regarding the impact on secretory granule biogenesis. These  
748 observations strongly suggest again that CgA and PLD1-generated PA cooperate to trigger the  
749 formation of secretory granules in neuroendocrine cells.

750 Finally, it must be pointed out that a recent study based on *in vitro* reconstitution  
751 assays and molecular modeling reported additional functions of specific species of PA during  
752 COPI vesicle fission (53). Indeed, PA generated by lysophosphatidic acid acyltransferase type  
753 gamma promotes the early stage of COPI vesicle fission whereas PA generated by  
754 phospholipase D type 2 promotes the late stage of fission. Intriguingly, PA with shorter fatty  
755 acid chains better supported the later function of PA, most likely by triggering the activity of  
756 BARS (53). It is of note that our lipidomic analysis indicates that these shorter forms of PA  
757 are scarce in Golgi or secretory granule membranes suggesting that only a tiny fraction of PA

758 could trigger the fission of budding vesicle, while larger proportion of PA is required for  
759 budding. A recent study revealed that PI4P in the cytosolic leaflet of the TGN membrane  
760 recruits cytosolic proteins such as GOLPH3 through its membrane curvature ability (54),  
761 suggesting that PA could also initiate this process by activating Golgi PIP-kinase to produce  
762 PI4P in the cytosolic leaflet.

763 Altogether, our data show that CgA binds to specific species of PA which in turn  
764 could act as lipid cofactors (55) at the TGN to induce membrane remodeling and curvature in  
765 order to initiate secretory granule budding, concomitantly or prior to the recruitment of  
766 cytosolic proteins such as GOLPH3 (54), arfaptins (56, 57), the acto-myosin 1b complex (58)  
767 or the membrane-associated myristoylated protein HID1 (59), but also small GTPase of the  
768 Arf family (60), all of which are also essential actors in this fundamental biological process  
769 necessary for regulated secretion. Further studies are now needed to evaluate the connection  
770 of CgA/PA interaction with the additional machinery involved in secretory granule  
771 biogenesis, in living neuroendocrine cells, and the potential implication of this interaction in  
772 diseases related to hormone secretion deregulation.

773

#### 774 **ACKNOWLEDGEMENTS**

775 We thank Jérôme Leprince for fruitful discussion for PABD modelization. This work was  
776 supported by institutional funding from INSERM, University of Rouen-Normandie, IBiSA,  
777 IRIB, Région Normandie, the European Regional Development Funds (ERDF DO-IT2015  
778 and ERDF – PACT-CBS programs), and grant from the Medical Research Foundation (FRM)  
779 (project number DEI20151234424) to MM-H, P-YR and NV. OC and CD-D were supported  
780 by fellowships from the Ministère de la Recherche et de l'Enseignement Supérieur. FL is co-  
781 supported by European Union and Région Normandie. LR was supported by fellowship from  
782 FRM. Lipidomic analyses were performed on the Bordeaux Metabolome Facility-  
783 MetaboHUB (ANR-11-INBS-0010). The authors declare that no competing interests exist.

784

#### 785 **AUTHOR CONTRIBUTIONS**

786 OC, FL and LR: designed and performed most of the experiments, analyzed the data and  
787 contributed to writing of the paper. CD-D: performed and analyzed lipid overlay assays. QW:  
788 performed some immunofluorescence and electron microscopy experiments and associated  
789 quantifications. ET and TT: performed the experiments related to liposome flotation and

790 binding assays. LJ: managed cell line culture and secretion experiments. DC: contributed to  
791 CgA-GFP and CgA $\Delta$ PABD-GFP cloning. AMH: performed electron microscopy experiments  
792 and associated quantifications. LF: performed the lipidome analysis using LC-MS/MS. OR,  
793 AH and P-YR: produced CgA coupled to Alexa Fluor 488 dye. DS and LG: performed super-  
794 resolution observations using STED nanoscope. YG: synthesized recombinant CgA. SA:  
795 designed AFM and ITC setup, and analyzed AFM and ITC data. NV: designed liposome  
796 flotation and binding assays, analyzed data from electron microscopy experiments, performed  
797 PA-binding domain prediction, and contributed to writing of the paper. YA: contributed to  
798 experiment design, data analysis and interpretation, and writing of the paper. MM-H:  
799 coordinated the study, designed, analyzed and interpreted data, and wrote the paper.

800

## 801 REFERENCES

- 802 1. Tanguy, E., Carmon, O., Wang, Q., Jeandel, L., Chasserot-Golaz, S., Montero-  
803 Hadjadje, M., and Vitale, N. (2016) Lipids implicated in the journey of a secretory  
804 granule: from biogenesis to fusion. *J. Neurochem.* **137**, 904–912
- 805 2. Holthuis, J. C. M. and Menon, A. K. (2014) Lipid landscapes and pipelines in  
806 membrane homeostasis. *Nature* **510**, 48–57
- 807 3. Surma, M. A., Klose, C., and Simons, K. (2012) Lipid-dependent protein sorting at the  
808 trans-Golgi network. *Biochim. Biophys. Acta - Mol. Cell Biol. Lipids* **1821**, 1059–1067
- 809 4. Dhanvantari, S., Arnaoutova, I., Snell, C. R., Steinbach, P. J., Hammond, K., Caputo,  
810 G. A., London, E., and Loh, Y. P. (2002) Carboxypeptidase E, a prohormone sorting  
811 receptor, is anchored to secretory granules via a C-terminal transmembrane insertion.  
812 *Biochemistry* **41**, 52–60
- 813 5. Gondré-Lewis, M. C., Petrache, H. I., Wassif, C. A., Harries, D., Parsegian, A., Porter,  
814 F. D., and Loh, Y. P. (2006) Abnormal sterols in cholesterol-deficiency diseases cause  
815 secretory granule malformation and decreased membrane curvature. *J. Cell Sci.* **119**,  
816 1876–1885
- 817 6. Duran, J. M., Campelo, F., van Galen, J., Sachsenheimer, T., Sot, J., Egorov, M. V.,  
818 Rentero, C., Enrich, C., Polishchuk, R. S., Goñi, F. M., Brügger, B., Wieland, F., and  
819 Malhotra, V. (2012) Sphingomyelin organization is required for vesicle biogenesis at  
820 the Golgi complex. *EMBO J.* **31**, 4535–4546

- 821 7. Makowski, S. L., Kuna, R. S., and Field, S. J. (2019) Induction of membrane curvature  
822 by proteins involved in Golgi trafficking. *Adv. Biol. Regul.* 100661
- 823 8. Montero-Hadjadje, M., Vaingankar, S., Elias, S., Tostivint, H., Mahata, S. K., and  
824 Anouar, Y. (2008) Chromogranins A and B and secretogranin II: Evolutionary and  
825 functional aspects. *Acta Physiol.* **192**, 309–324
- 826 9. Chanat, E. and Huttner, W. B. (1991) Milieu-induced, selective aggregation of  
827 regulated secretory proteins in the trans-Golgi network. *J. Cell Biol.* **115**, 1505–1519
- 828 10. Kim, T., Tao-Cheng, J. H., Eiden, L. E., and Loh, Y. P. (2001) Chromogranin A, an  
829 “on/off” switch controlling dense-core secretory granule biogenesis. *Cell* **106**, 499–509
- 830 11. Elias, S., Delestre, C., Courel, M., Anouar, Y., and Montero-Hadjadje, M. (2010)  
831 Chromogranin A as a crucial factor in the sorting of peptide hormones to secretory  
832 granules. *Cell. Mol. Neurobiol.* **30**, 1189–1195
- 833 12. Mahapatra, N. R., O’Connor, D. T., Vaingankar, S. M., Hikim, A. P. S., Mahata, M.,  
834 Ray, S., Staite, E., Wu, H., Gu, Y., Dalton, N., Kennedy, B. P., Ziegler, M. G., Ross, J.,  
835 and Mahata, S. K. (2005) Hypertension from targeted ablation of chromogranin A can  
836 be rescued by the human ortholog. *J. Clin. Invest.* **115**, 1942–1952
- 837 13. Bandyopadhyay, G. K. and Mahata, S. K. (2017) Chromogranin A Regulation of  
838 Obesity and Peripheral Insulin Sensitivity. *Front. Endocrinol. (Lausanne)*. **8**, 20
- 839 14. Montero-Hadjadje, M., Elias, S., Chevalier, L., Benard, M., Tanguy, Y., Turquier, V.,  
840 Galas, L., Yon, L., Malagon, M. M., Driouich, A., Gasman, S., and Anouar, Y. (2009)  
841 Chromogranin A promotes peptide hormone sorting to mobile granules in  
842 constitutively and regulated secreting cells. Role of conserved N- and C-terminal  
843 peptides. *J. Biol. Chem.* **284**, 12420–12431
- 844 15. Elias, S., Delestre, C., Ory, S., Marais, S., Courel, M., Vazquez-Martinez, R., Bernard,  
845 S., Coquet, L., Malagon, M. M., Driouich, A., Chan, P., Gasman, S., Anouar, Y., and  
846 Montero-Hadjadje, M. (2012) Chromogranin A induces the biogenesis of granules with  
847 calcium- and actin-dependent dynamics and exocytosis in constitutively secreting cells.  
848 *Endocrinology* **153**, 4444–4456
- 849 16. Kang, Y. K. and Yoo, S. H. (1997) Identification of the secretory vesicle membrane  
850 binding region of chromogranin A. *FEBS Lett.* **404**, 87–90

- 851 17. Abbineni, P. S., Bittner, M. A., Axelrod, D., and Holz, R. W. (2019) Chromogranin A,  
852 the major luminal protein in chromaffin granules, controls fusion pore expansion. *J.*  
853 *Gen. Physiol.* **151**, 118–130
- 854 18. Blois, A., Holmsen, H., Martino, G., Corti, A., Metz-Boutigue, M. H., and Helle, K. B.  
855 (2006) Interactions of chromogranin A-derived vasostatins and monolayers of  
856 phosphatidylserine, phosphatidylcholine and phosphatidylethanolamine. *Regul. Pept.*  
857 **134**, 30–37
- 858 19. Dondossola, E., Gasparri, A., Bachi, A., Longhi, R., Metz-Boutigue, M.-H., Tota, B.,  
859 Helle, K. B., Curnis, F., and Corti, A. (2010) Role of vasostatin-1 C-terminal region in  
860 fibroblast cell adhesion. *Cell. Mol. Life Sci.* **67**, 2107–2118
- 861 20. Sugawara, M., Resende, J. M., Moraes, C. M., Marquette, A., Chich, J.-F., Metz-  
862 Boutigue, M.-H., and Bechinger, B. (2010) Membrane structure and interactions of  
863 human catestatin by multidimensional solution and solid-state NMR spectroscopy.  
864 *FASEB J.* **24**, 1737–1746
- 865 21. Kassas, N., Tanguy, E., Thahouly, T., Fouillen, L., Heintz, D., Chasserot-Golaz, S.,  
866 Bader, M.-F., Grant, N. J., and Vitale, N. (2017) Comparative Characterization of  
867 Phosphatidic Acid Sensors and Their Localization during Frustrated Phagocytosis. *J.*  
868 *Biol. Chem.* **292**, 4266–4279
- 869 22. Ammar, M.-R., Humeau, Y., Hanauer, A., Nieswandt, B., Bader, M.-F., and Vitale, N.  
870 (2013) The Coffin-Lowry Syndrome-Associated Protein RSK2 Regulates Neurite  
871 Outgrowth through Phosphorylation of Phospholipase D1 (PLD1) and Synthesis of  
872 Phosphatidic Acid. *J. Neurosci.* **33**, 19470–19479
- 873 23. Ammar, M. R., Thahouly, T., Hanauer, A., Stegner, D., Nieswandt, B., and Vitale, N.  
874 (2015) PLD1 participates in BDNF-induced signalling in cortical neurons. *Sci. Rep.* **5**,  
875 14778
- 876 24. Chevalier, A., Massif, C., Renard, P.-Y., and Romieu, A. (2013) Bioconjugatable Azo-  
877 Based Dark-Quencher Dyes: Synthesis and Application to Protease-Activatable Far-  
878 Red Fluorescent Probes. *Chemistry* **19**, 1686–1699
- 879 25. Montero-Hadjadje, M., Vaudry, H., Turquier, V., Leprince, J., Do Rego, J.-L., Yon, L.,  
880 Gallo-Payet, N., Plouin, P.-F., and Anouar, Y. (2002) Localization and characterization  
881 of evolutionarily conserved chromogranin A-derived peptides in the rat and human

- 882 pituitary and adrenal glands. *Cell Tissue Res.* **310**, 223–236
- 883 26. Anouar, Y., Desmoucelles, C., Yon, L., Leprince, J., Breault, L., Gallo-Payet, N., and  
884 Vaudry, H. (1998) Identification of a Novel Secretogranin II-Derived Peptide (SgII<sub>187–</sub>  
885 <sub>252</sub>) in Adult and Fetal Human Adrenal Glands Using Antibodies Raised against the  
886 Human Recombinant Peptide. *J. Clin. Endocrinol. Metab.* **83**, 2944–2951
- 887 27. Graham, J. M. (2001) Isolation of Golgi Membranes from Tissues and Cells by  
888 Differential and Density Gradient Centrifugation. *Curr. Protoc. Cell Biol.* **10**, 3.9.1-  
889 3.9.24
- 890 28. Bligh, E. G. and Dyer, W. J. (1959) A rapid method of total lipid extraction and  
891 purification. *Can. J. Biochem. Physiol.* **37**, 911–917
- 892 29. Shui, G., Guan, X. L., Low, C. P., Chua, G. H., Goh, J. S. Y., Yang, H., and Wenk, M.  
893 R. (2010) Toward one step analysis of cellular lipidomes using liquid chromatography  
894 coupled with mass spectrometry: application to *Saccharomyces cerevisiae* and  
895 *Schizosaccharomyces pombe* lipidomics. *Mol. Biosyst.* **6**, 1008
- 896 30. Bénard, M., Schapman, D., Lebon, A., Monterroso, B., Bellenger, M., Le Foll, F.,  
897 Pasquier, J., Vaudry, H., Vaudry, D., and Galas, L. (2015) Structural and functional  
898 analysis of tunneling nanotubes (TnTs) using gCW STED and gconfocal approaches.  
899 *Biol. cell* **107**, 419–425
- 900 31. Galas, L., Gallavardin, T., Bénard, M., Lehner, A., Schapman, D., Lebon, A., Komuro,  
901 H., Lerouge, P., Leleu, S., and Franck, X. (2018) “Probe, Sample, and Instrument  
902 (PSI)”: The Hat-Trick for Fluorescence Live Cell Imaging. *Chemosensors* **6**, 40
- 903 32. Huston, E., Gall, I., Houslay, T. M., and Houslay, M. D. (2006) Helix-1 of the cAMP-  
904 specific phosphodiesterase PDE4A1 regulates its phospholipase-D-dependent  
905 redistribution in response to release of Ca<sup>2+</sup>. *J. Cell Sci.* **119**, 3799–3810
- 906 33. Gautier, R., Douguet, D., Antony, B., and Drin, G. (2008) HELIQUEST: a web server  
907 to screen sequences with specific alpha-helical properties. *Bioinformatics* **24**, 2101–  
908 2102
- 909 34. Tanguy, E., Kassas, N., and Vitale, N. (2018) Protein–Phospholipid Interaction Motifs:  
910 A Focus on Phosphatidic Acid. *Biomolecules* **8**, 20
- 911 35. Pierce, M. M., Raman, C. S., and Nall, B. T. (1999) Isothermal titration calorimetry of

- 912 protein-protein interactions. *Methods* **19**, 213–221
- 913 36. Miao, R., Lung, S.-C., Li, X., Li, X. D., and Chye, M.-L. (2019) Thermodynamic  
914 insights into an interaction between acyl-coa-binding protein2 and lysophospholipase2  
915 in *Arabidopsis*. *J. Biol. Chem.* **294**, 6214–6226
- 916 37. Freyberg, Z., Siddhanta, A., and Shields, D. (2003) "Slip, sliding away": phospholipase  
917 D and the Golgi apparatus. *Trends Cell Biol.* **13**, 540–546
- 918 38. Freyberg, Z., Sweeney, D., Siddhanta, A., Bourgoin, S., Frohman, M., and Shields, D.  
919 (2001) Intracellular Localization of Phospholipase D1 in Mammalian Cells. *Mol. Biol.*  
920 *Cell* **12**, 943–955
- 921 39. Gondré-Lewis, M. C., Park, J. J., and Loh, Y. P. (2012) Cellular mechanisms for the  
922 biogenesis and transport of synaptic and dense-core vesicles. *Int. Rev. Cell Mol. Biol.*  
923 **299**, 27–115
- 924 40. Siddhanta, A. and Shields, D. (1998) Secretory vesicle budding from the trans-Golgi  
925 network is mediated by phosphatidic acid levels. *J. Biol. Chem.* **273**, 17995–17998
- 926 41. Cullis, P. R., Hope, M. J., Bally, M. B., Madden, T. D., Mayer, L. D., and Fenske, D.  
927 B. (1997) Influence of pH gradients on the transbilayer transport of drugs, lipids,  
928 peptides and metal ions into large unilamellar vesicles. *Biochim. Biophys. Acta* **1331**,  
929 187–211
- 930 42. Pomorski, T. G. and Menon, A. K. (2016) Lipid somersaults: Uncovering the  
931 mechanisms of protein-mediated lipid flipping. *Prog. Lipid Res.* **64**, 69–84
- 932 43. Braks, J. A. M. and Martens, G. J. M. (1994) 7B2 is a neuroendocrine chaperone that  
933 transiently interacts with prohormone convertase PC2 in the secretory pathway. *Cell*  
934 **78**, 263–273
- 935 44. Aunis, D. and Metz-Boutigue, M. H. (2001) Chromogranines: De la découverte à la  
936 fonction. *Medecine/Sciences* **17**, 418–427
- 937 45. Taupenot, L., Harper, K. L., and O'Connor, D. T. (2003) The Chromogranin–  
938 Secretogranin Family. *N. Engl. J. Med.* **348**, 1134–1149
- 939 46. Potocký, M., Pleskot, R., Pejchar, P., Vitale, N., Kost, B., and Žárský, V. (2014) Live-  
940 cell imaging of phosphatidic acid dynamics in pollen tubes visualized by Spo20p-

- 941 derived biosensor. *New Phytol.* **203**, 483–494
- 942 47. Kooijman, E. E., Chupin, V., de Kruijff, B., and Burger, K. N. J. (2003) Modulation of  
943 membrane curvature by phosphatidic acid and lysophosphatidic acid. *Traffic* **4**, 162–  
944 174
- 945 48. Sahu, B. S., Obbineni, J. M., Sahu, G., Allu, P. K. R., Subramanian, L., Sonawane, P.  
946 J., Singh, P. K., Sasi, B. K., Senapati, S., Maji, S. K., Bera, A. K., Gomathi, B. S.,  
947 Mulasari, A. S., and Mahapatra, N. R. (2012) Functional Genetic Variants of the  
948 Catecholamine-Release-Inhibitory Peptide Catestatin in an Indian Population. *J. Biol.*  
949 *Chem.* **287**, 43840–43852
- 950 49. Kiranmayi, M., Chirasani, V. R., Allu, P. K. R., Subramanian, L., Martelli, E. E., Sahu,  
951 B. S., Vishnuprabu, D., Kumaragurubaran, R., Sharma, S., Bodhini, D., Dixit, M.,  
952 Munirajan, A. K., Khullar, M., Radha, V., Mohan, V., Mulasari, A. S., Naga Prasad, S.  
953 V., Senapati, S., and Mahapatra, N. R. (2016) Catestatin Gly364Ser Variant Alters  
954 Systemic Blood Pressure and the Risk for Hypertension in Human Populations via  
955 Endothelial Nitric Oxide Pathway. *Hypertension* **68**, 334–347
- 956 50. Riebeling, C., Morris, A. J., and Shields, D. (2009) Phospholipase D in the Golgi  
957 apparatus. *Biochim. Biophys. Acta* **1791**, 876–880
- 958 51. Vitale, N., Caumont, A. S., Chasserot-Golaz, S., Du, G., Wu, S., Sciorra, V. A., Morris,  
959 A. J., Frohman, M. A., and Bader, M. F. (2001) Phospholipase D1: a key factor for the  
960 exocytotic machinery in neuroendocrine cells. *EMBO J.* **20**, 2424–2434
- 961 52. Pasqua, T., Mahata, S., Bandyopadhyay, G. K., Biswas, A., Perkins, G. A., Sinha-  
962 Hikim, A. P., Goldstein, D. S., Eiden, L. E., and Mahata, S. K. (2016) Impact of  
963 Chromogranin A deficiency on catecholamine storage, catecholamine granule  
964 morphology and chromaffin cell energy metabolism in vivo. *Cell Tissue Res.* **363**, 693–  
965 712
- 966 53. Park, S. Y., Yang, J. S., Li, Z., Deng, P., Zhu, X., Young, D., Ericsson, M., Andringa,  
967 R. L. H., Minnaard, A. J., Zhu, C., Sun, F., Moody, D. B., Morris, A. J., Fan, J., and  
968 Hsu, V. W. (2019) The late stage of COPI vesicle fission requires shorter forms of  
969 phosphatidic acid and diacylglycerol. *Nat. Commun.* **10**, 1–14
- 970 54. Rahajeng, J., Kuna, R. S., Makowski, S. L., Tran, T. T. T., Buschman, M. D., Li, S.,  
971 Cheng, N., Ng, M. M., and Field, S. J. (2019) Efficient Golgi Forward Trafficking

- 972 Requires GOLPH3-Driven, PI4P-Dependent Membrane Curvature. *Dev. Cell* **50**, 573–  
973 585
- 974 55. Zhukovsky, M. A., Filograna, A., Luini, A., Corda, D., and Valente, C. (2019) Protein  
975 Amphipathic Helix Insertion : A Mechanism to Induce Membrane Fission. *Front. Cell*  
976 *Dev. Biol.* **7**, 1–29
- 977 56. Cruz-Garcia, D., Ortega-Bellido, M., Scarpa, M., Villeneuve, J., Jovic, M., Porzner,  
978 M., Balla, T., Seufferlein, T., and Malhotra, V. (2013) Recruitment of arfaptins to the  
979 trans-Golgi network by PI(4)P and their involvement in cargo export. *EMBO J.* **32**,  
980 1717–1729
- 981 57. Gehart, H., Goginashvili, A., Beck, R., Morvan, J., Erbs, E., Formentini, I., De Matteis,  
982 M. A., Schwab, Y., Wieland, F. T., and Ricci, R. (2012) The BAR Domain Protein  
983 Arfaptin-1 Controls Secretory Granule Biogenesis at the trans-Golgi Network. *Dev.*  
984 *Cell* **23**, 756–768
- 985 58. Delestre-Delacour, C., Carmon, O., Laguerre, F., Estay-Ahumada, C., Courel, M.,  
986 Elias, S., Jeandel, L., Rayo, M. V., Peinado, J. R., Sengmanivong, L., Gasman, S.,  
987 Coudrier, E., Anouar, Y., and Montero-Hadjadje, M. (2017) Myosin 1b and F-actin are  
988 involved in the control of secretory granule biogenesis. *Sci. Rep.* **7**, 5172
- 989 59. Hummer, B. H., de Leeuw, N. F., Burns, C., Chen, L., Joens, M. S., Hosford, B.,  
990 Fitzpatrick, J. A. J., and Asensio, C. S. (2017) HID-1 controls formation of large dense  
991 core vesicles by influencing cargo sorting and trans-Golgi network acidification. *Mol.*  
992 *Biol. Cell* **28**, 3870–3880
- 993 60. Vitale, N., Chasserot-Golaz, S., Bailly, Y., Morinaga, N., Frohman, M. A., and Bader,  
994 M. F. (2002) Calcium-regulated exocytosis of dense-core vesicles requires the  
995 activation of ADP-ribosylation factor (ARF)6 by ARF nucleotide binding site opener at  
996 the plasma membrane. *J. Cell Biol.* **159**, 79–89

997

998

## 999 **FIGURE LEGENDS**

1000 **Figure 1.** CgA interacts with PA through a putative PABD and Golgi PA is involved in CgA  
1001 secretory granule biogenesis.

1002 A Protein–lipid overlay assay in the presence of recombinant CgA (500 ng/ml) using  
1003 commercial membrane strips where 100 pmol/spot of the following lipids are adsorbed:  
1004 triglycerides, diacylglycerol (DAG), phosphatidic acid (PA), phosphatidylserine (PS),  
1005 phosphatidylethanolamine (PE), phosphatidylcholine (PC), phosphatidylglycerol (PG),  
1006 cardiolipin, phosphatidylinositol (PI), phosphatidylinositol 4-phosphate (PI(4)P),  
1007 phosphatidylinositol 4,5-bisphosphate (PI(4,5)P<sub>2</sub>), phosphatidylinositol 3,4,5-trisphosphate  
1008 (PI(3,4,5)P<sub>3</sub>), cholesterol, sphingomyelin, or 3-sulfogalactosylceramide (sulfatide). After  
1009 the overlay, the membrane was immunostained for CgA using the anti-WE-14 antibody,  
1010 and revealed using a chemiluminescence kit. Plotted are means of CgA binding intensity  
1011 expressed as percentage normalized to control (blank)  $\pm$  s.e.m. (n=3). \*\*\* $P < 0.001$ , Anova  
1012 one-way analysis of variance test with Bonferroni’s comparison test.

1013 B Involvement of Golgi PA in the formation of CgA-containing secretory granules in PC12  
1014 cells. Cells expressing wild-type PDE4A1 coupled with GFP (PDE4A1(PABD)) or PABD-  
1015 mutated PDE4A1 coupled with GFP (PDE4A1(PABD Mut)) are surrounded by a dashed  
1016 line. Cells were immunolabelled with anti-CgA antibody and their fluorescence was  
1017 examined using confocal microscopy. Representative confocal microscopy sections  
1018 throughout the cells are shown. Values for the intensity of CgA staining and the number of  
1019 granules per cell are plotted as the means  $\pm$  S.D. (n=2; 40 cells per condition). \*\* $P < 0.01$ ,  
1020 Mann-Whitney test. The scale bar represents 20  $\mu$ m. Western blots show expression of  
1021 CgA and  $\alpha$ -tubulin as loading control.

1022 C Human CgA (hCgA) sequence showing a region of 18 amino acids (364-381),  
1023 encompassing a positive charge cluster and hydrophobic residues that could adopt an  $\alpha$ -  
1024 helical conformation, delimited by arrows, suggesting its function as PA-binding domain  
1025 (PABD).

1026 D PA binding profile of the putative human CgA-PABD. Amphipathic  $\alpha$ -helix projection of  
1027 the core 18 amino acids of the PABD of CgA obtained with Heliquest software. Arrow  
1028 indicates hydrophobic moment. Red N and C indicate the beginning and the end of PABD  
1029 amino acid sequence.

1030 E Model of the putative human CgA-PABD. Ribbon corresponds to the  $\alpha$ -helix. The  
1031 structure was determined using MacPyMOL (v1.74).

1032 F Characterization of the PA binding capacity of human CgA through the putative PABD.  
1033 Semi-quantitative fluorescent liposome assays with fluorescent liposomes (5% PE-NBD,  
1034 95% DOPC) or PA-containing fluorescent liposomes (5% PE-NBD, 85% DOPC, 10% PA  
1035 mix) and GST-CgA-PABD constructs linked to GSH-sepharose beads. The binding of  
1036 liposomes with CgA-PABD constructs was monitored by fluorimetry. Results are  
1037 presented as means  $\pm$  S.D. (triplicate measurements; n=3).

1038

1039 **Figure 2.** Same predominant PA species are found in Golgi and secretory granule membranes  
1040 from COS7-WT, COS7-CgA and PC12 cells.

1041 A The level of distinct PA species was measured in fractions of secretory granule (SG) and  
1042 Golgi membranes from COS7-CgA cells by duplicate UPLC/MS/MS analysis of two  
1043 samples (each containing 200  $\mu$ g of protein) from each fraction. The acyl chain  
1044 composition of each species is shown on the x axis. The y axis shows the abundance of  
1045 each species as a percentage of total PA in the sample.

1046 B PA levels were measured in fractions of Golgi membranes from COS7-WT or COS7-CgA  
1047 cells by duplicate UPLC/MS/MS analysis of two samples (each containing 200  $\mu$ g of  
1048 protein) from each fraction. The acyl chain composition of each species is shown on the x  
1049 axis. The y axis shows the abundance of each species as a percentage of total PA in the  
1050 sample.

1051 C PA levels were measured in secretory granule-containing fractions from PC12 or COS7-  
1052 CgA cells by duplicate UPLC/MS/MS analysis of two samples (each containing 200  $\mu$ g of  
1053 protein) from each fraction. The acyl chain composition of each species is shown on the x  
1054 axis. The y axis shows the abundance of each species as a percentage of total PA in the  
1055 sample.

1056

1057 **Figure 3.** CgA interacts with PA species identified in Golgi and secretory granule membranes  
1058 and provokes membrane deformation of PA-enriched GUVs.

1059 A Schematic representation of the liposome flotation assay approach used to study the  
1060 interaction of CgA from COS7-CgA cell extracts with PA species.

1061 B Detection of CgA in the different fractions (Top (T), Medium (M), Bottom (B)) obtained  
1062 from liposome assays. COS7-CgA cell extracts were incubated with liposomes containing  
1063 5% PE-NBD, 85% of DOPC, and 10% of the indicated phosphatidylcholine (PC),  
1064 phosphatidylserine (PS), phosphatidylinositol-4,5-bisphosphate (PIP2), a commercial

1065 phosphatidic acid mix (PA) or distinct species of PA (PA(36:0), PA(36:1) or PA(40:6)).  
1066 Thirty µg of protein from each fraction were run on SDS-PAGE and immunoblotted with  
1067 the WE-14 antibody.

1068 C Formation of fluorescent PA-containing GUVs by PVA-assisted swelling. Stable  
1069 fluorescent GUVs (95% DOPC, 4% PA(36:1) and 1% PE-NBD) were generated and  
1070 observed by live confocal microscopy during 1 min. Representative confocal microscopy  
1071 sections throughout the GUVs are shown. The scale bar represents 30 µm.

1072 D Effect of CgA on fluorescent PA-containing GUVs. Fluorescent GUVs (95% DOPC, 4%  
1073 PA(36:1) or PA(40:6) and 1% PE-NBD) were incubated with 2 µM CgA. Deformation of  
1074 GUV membrane (arrows) was observed by live confocal microscopy during 1 min.  
1075 Representative confocal microscopy sections throughout the GUVs are shown. The scale  
1076 bar represents 30 µm.

1077 E Quantification of generated vesicles following membrane deformation of PA-containing  
1078 GUVs. GUVs (95% DOPC, 4% PA(36:1), 1% PE-NBD) were incubated with 2, 4 and 6  
1079 µM CgA (n=3; 35 videos per condition). \*\*\* $P < 0.001$ , Mann-Whitney test. Means  $\pm$  s.e.m.  
1080 are plotted.

1081 F Distribution of CgA-Alexa488 on PA-containing GUVs. GUVs (96% DOPC, 4%  
1082 PA(36:1)) were incubated with 2 µM CgA-Alexa488. Staining and budding (arrows) of  
1083 GUV membrane was observed by live confocal microscopy during 1 min. Representative  
1084 confocal microscopy sections throughout the GUVs are shown. The scale bar represents  
1085 20 µm.

1086

1087 **Figure 4.** ITC analysis reveals that PA favors membrane incorporation of CgA.

1088 A DOPC SUVs and CgA binding measured by titrating 5 µM CgA in the chamber with 10  
1089 mM vesicle suspension in the syringe. Top panel, raw heating power over time obtained  
1090 with DOPC SUV injection in water; bottom panel, raw heating power over time obtained  
1091 with DOPC SUV injection in CgA solution.

1092 B DOPC/PA(36:1) SUVs and CgA binding measured by titrating 5 µM CgA in the chamber  
1093 with 10 mM vesicle suspension in the syringe. Top panel, raw heating power over time  
1094 obtained with DOPC/PA(36:1) SUV injection in water; bottom panel, raw heating power  
1095 over time obtained with DOPC/PA(36:1) SUV injection in CgA solution.

1096 C Fit curves of the integrated energy values obtained from A and B traces in bottom panels  
1097 using A and B traces in top panels as blank, respectively. Experiments were carried out at  
1098 10°C, and each value is the mean of three independent titrations.

1099

1100 **Figure 5.** CgA induces the remodeling of PA-enriched membrane bilayers.

1101 A Atomic force microscopy topographical images of mica supported bilayer surfaces from  
1102 DOPC GUVs, incubated without or with 0.6 and 1.2  $\mu\text{M}$  CgA, during 15 min (T1) and 75  
1103 min (T2). The scale bar represents 2  $\mu\text{m}$ . The scheme corresponds to a topographical  
1104 profile through an aggregate (enlarged view) showing a difference of height of 6 nm with  
1105 the continuous phase.

1106 B Atomic force microscopy topographical images of mica supported bilayer surfaces from  
1107 DOPC/PA(36:1) (9:1, mol ratio) GUVs, incubated without or with 0.6 and 1.2  $\mu\text{M}$  CgA,  
1108 during 15 min (T1) and 75 min (T2). Arrow heads indicate aggregates that appeared at T1  
1109 and are maintained at T2; arrows indicate aggregates that appeared between T1 and T2.  
1110 The scale bar represents 2  $\mu\text{m}$ . The scheme corresponds to topographical profiles through  
1111 aggregates (enlarged views) showing a difference of height of 6 nm (a) and 17 nm (b) with  
1112 the continuous phase.

1113

1114 **Figure 6.** Number, surface and height of CgA-induced domains depend on PA enrichment of  
1115 membrane bilayers.

1116 A Scatter plot showing the number, area and height of domains obtained after incubation of  
1117 supported bilayer surfaces from DOPC GUVs with 1.2  $\mu\text{M}$  CgA during 75 min. Insert  
1118 corresponds to enlarged view of the delimited zone emphasizing domains with height  
1119 below 4 nm and area below 6,000  $\text{nm}^2$  (within blue surrounded zone). Analysis of domains  
1120 was performed on 15 images and domains detected on an image are of the same color.

1121 B Scatter plot showing the number, area and height of domains obtained after incubation of  
1122 supported bilayer surfaces from DOPC/PA(36:1) (9:1, mol ratio) GUVs with 1.2  $\mu\text{M}$  CgA  
1123 during 75 min. Insert corresponds to enlarged view of the delimited zone emphasizing  
1124 domains with height below 4 nm and area below 6,000  $\text{nm}^2$  (within blue surrounded zone).  
1125 Analysis of domains was performed on 11 images and domains detected on an image are  
1126 of the same color.

1127

1128 **Figure 7.** CgA PABD is required for secretory granule biogenesis.

1129 A COS-7 cells transfected with plasmids encoding full-length CgA-GFP or CgA PABD-  
1130 mutated form (CgA $\Delta$ PABD)-GFP were examined for GFP fluorescence and GM130  
1131 immunoreactivity using confocal microscopy. Representative confocal microscopy  
1132 sections throughout the cells are shown and were used to quantify automatically the  
1133 granules with a diameter > 200 nm. Values for the number of granules/cell are plotted as  
1134 the means  $\pm$  s.e.m. (n=3; 65 cells per condition). \*\*\* $P$  < 0.001, Mann-Whitney test. The  
1135 scale bar represents 20  $\mu$ m. Western blots show expression of CgA-GFP or CgA $\Delta$ PABD-  
1136 GFP fusion proteins and  $\alpha$ -tubulin as loading control.

1137 B AtT20 cells transfected with plasmids encoding full-length CgA-GFP or CgA PABD-  
1138 mutated form (CgA $\Delta$ PABD)-GFP were examined for GFP fluorescence and GM130  
1139 immunoreactivity using confocal microscopy. Representative confocal microscopy  
1140 sections throughout the cells are shown and were used to quantify automatically the  
1141 granules with a diameter > 200 nm. Values for the number of granules/cell are plotted as  
1142 the means  $\pm$  s.e.m. (n=3; 70 cells per condition). \*\*\* $P$  < 0.001, Mann-Whitney test. The  
1143 scale bar represents 20  $\mu$ m. Western blots show expression of CgA-GFP or CgA $\Delta$ PABD-  
1144 GFP fusion proteins and  $\alpha$ -tubulin as loading control.

1145 C Golgi area of COS-7 cells transfected with plasmids encoding full-length CgA-GFP or  
1146 CgA PABD-mutated form (CgA $\Delta$ PABD)-GFP was examined for GFP fluorescence using  
1147 gCW STED. Representative sections are shown after deconvolution. The scale bar  
1148 represents 1  $\mu$ m.

1149 D Golgi area of AtT20 cells transfected with plasmids encoding full-length CgA-GFP or CgA  
1150 PABD-mutated form (CgA $\Delta$ PABD)-GFP was examined for GFP fluorescence using gCW  
1151 STED. Representative sections are shown after deconvolution. The scale bar represents  
1152 1  $\mu$ m.

1153

1154 **Figure 8.** Inhibition of PLD-mediated PA synthesis alters secretory granule biogenesis.

1155 A COS7-CgA cells were treated or not with 75 nM FIPI for 6 h, fixed and immunolabelled  
1156 with anti-GM130 and anti-CgA antibodies. Representative confocal microscopy sections  
1157 throughout the cells are shown. The scale bar represents 20  $\mu$ m. Values for the number of  
1158 CgA secretory granules are plotted as the means  $\pm$  s.e.m. (n=3; 60 cells per condition).

1159 \*\*\* $P < 0.001$ , Mann-Whitney test. Western blots show expression of CgA and  $\alpha$ -tubulin as  
1160 loading control.

1161 B PC12 cells were treated or not with 75 nM FIPI for 6 h, fixed and immunolabelled with  
1162 anti-GM130 and anti-CgA antibodies. Representative confocal microscopy sections  
1163 throughout the cells are shown. The scale bar represents 10  $\mu$ m. Values for the number of  
1164 CgA secretory granules are plotted as the means  $\pm$  s.e.m. (n=3; 60 cells per condition).  
1165 Mann-Whitney test. Western blots show expression of CgA, CgB and SgII proteins, and  $\alpha$ -  
1166 tubulin as loading control.

1167 C Electron microscopy analysis of chromaffin cells from WT (control) and *Pld1*<sup>-/-</sup> mice.  
1168 White arrows indicate representative secretory granules. The scale bars represent 2  $\mu$ m.

1169 D Quantification of the number of secretory granules (SG) shown in panel (A) (n=6 mice per  
1170 condition; 50 cells per mouse adrenal medulla). \* $P < 0.05$ , Mann-Whitney test.  
1171 Means  $\pm$  s.e.m. are plotted.

1172 E Quantification of the dense core diameter of secretory granules (SG) shown in panel (A)  
1173 (n=6 mice per condition; 950 granules). \* $P < 0.05$ , Mann-Whitney test. Means  $\pm$  s.e.m. are  
1174 plotted.

**Table 1.**

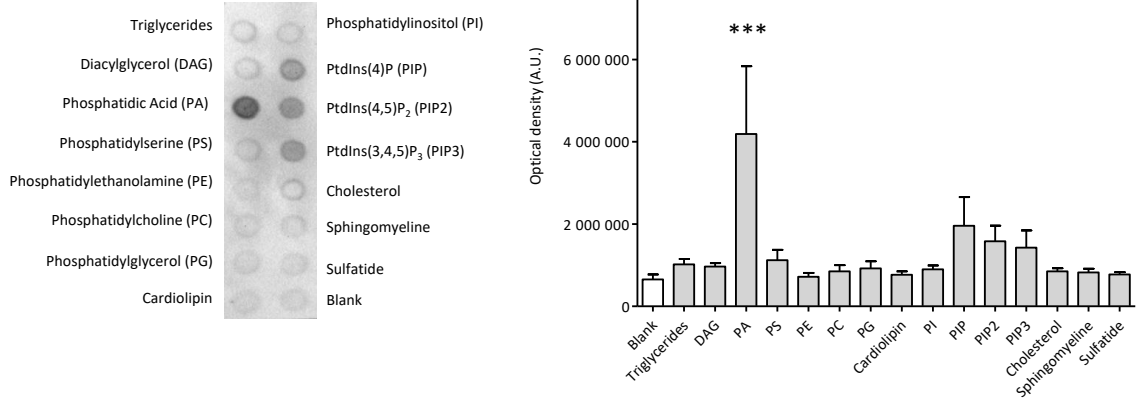
Thermodynamic parameters for CgA binding on DOPC and DOPC/PA(36:1) SUVs. The values are plotted in Fig. 4C.

	DOPC		DOPC / PA(36 :1)	
	exothermic	endothermic	exothermic	endothermic
Kd (M)	$1.5 \cdot 10^{-4} \pm 0.5 \cdot 10^{-4}$	$2 \cdot 10^{-5} \pm 1 \cdot 10^{-5}$	$1.16 \cdot 10^{-3} \pm 0.03 \cdot 10^{-3}$	$3 \cdot 10^{-4} \pm 0.1 \cdot 10^{-4}$
n	$259 \pm 30$	$460 \pm 40$	$199 \pm 5$	$355 \pm 5$
$\Delta H$ (kJ/mol)	$-1.82 \pm 0.09$	$0.640 \pm 0.06$	$-12.9 \pm 0.3$	$7.65 \pm 0.15$
$\Delta S$ (J/mol.K)	$67.3 \pm 3.2$	$93.4 \pm 4.8$	$10.6 \pm 1.3$	$94.5 \pm 0.8$

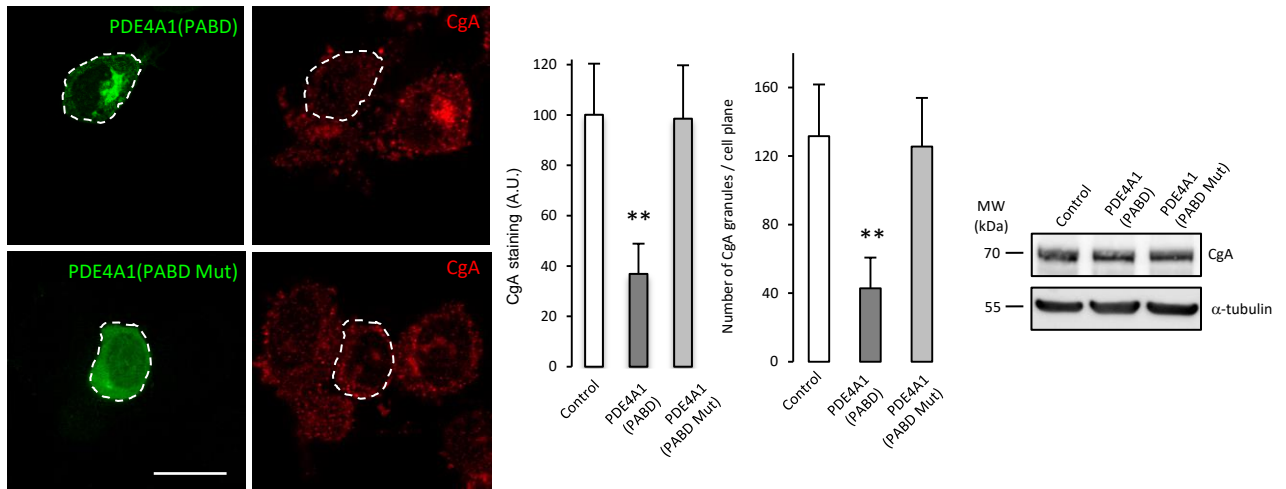
Experiments were carried out at 10°C, and each value is the mean  $\pm$  standard deviation from the fitted data of three independent experiments. Kd, dissociation constant; n, number of binding sites;  $\Delta H$ , enthalpy change;  $\Delta S$ , entropy change.

# Figure 1

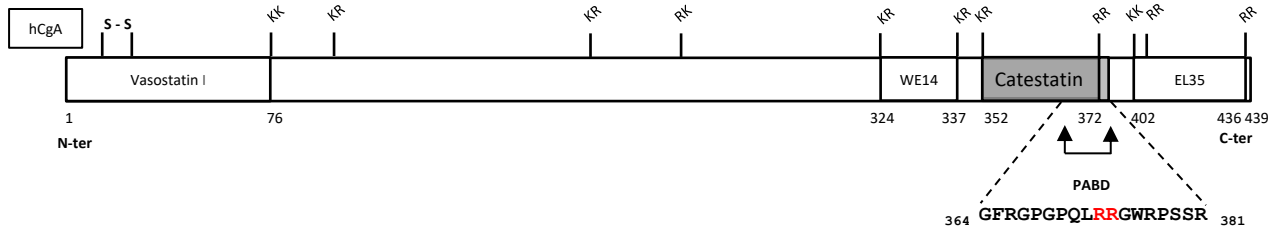
**A**



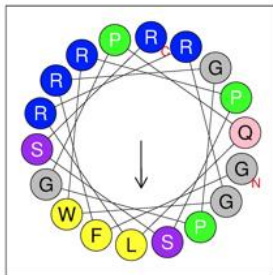
**B**



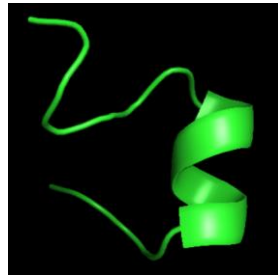
**C**



**D**



**E**



**F**

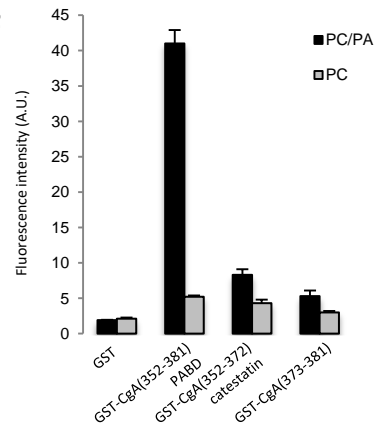
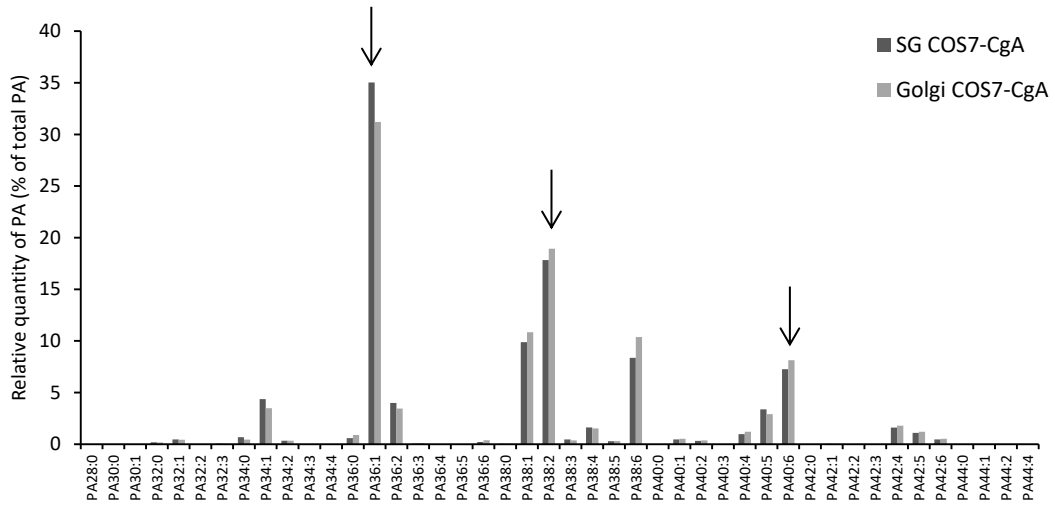


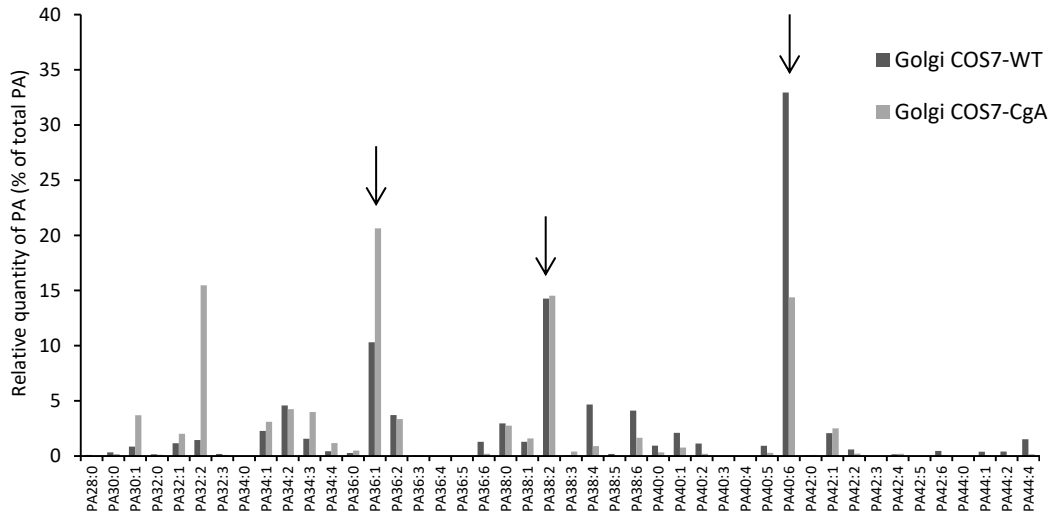
**Figure 1**

# Figure 2

**A**



**B**



**C**

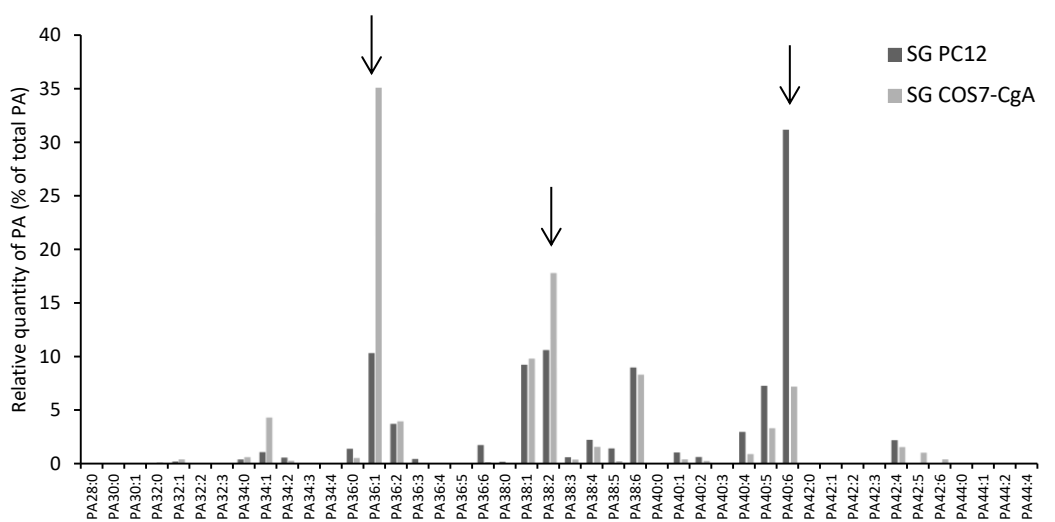
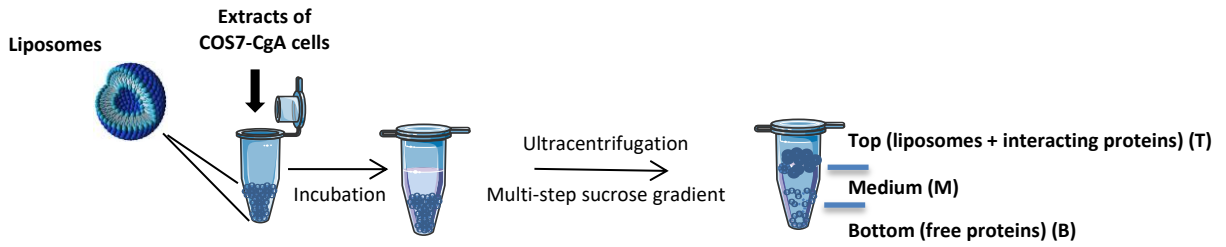
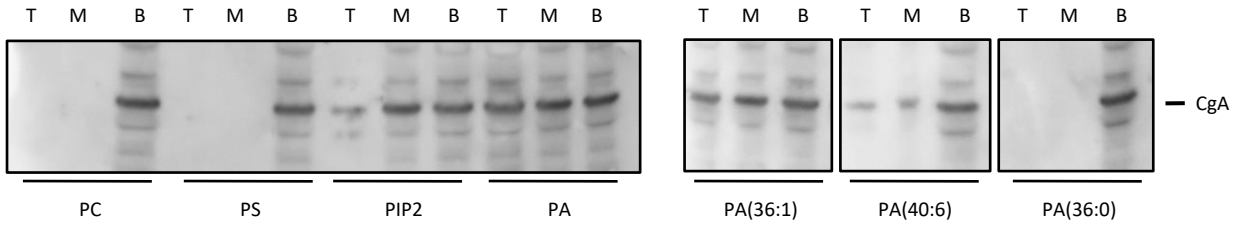


# Figure 3

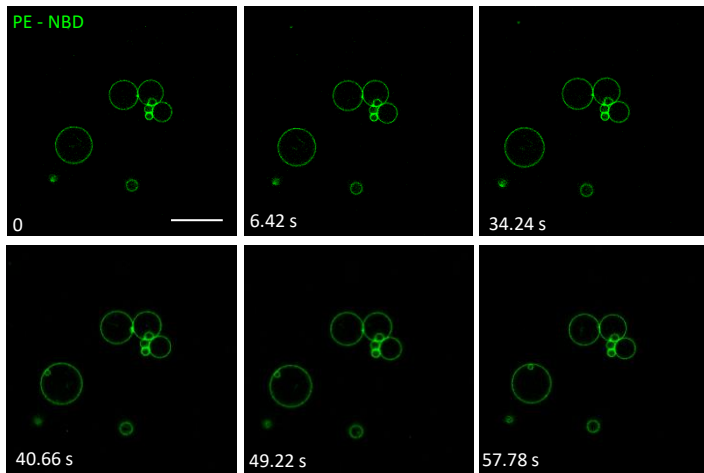
**A**



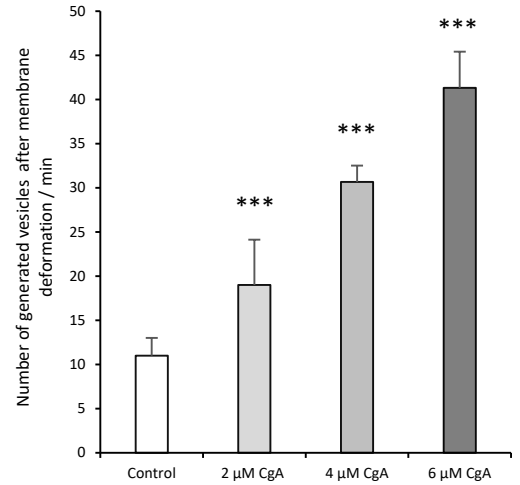
**B**



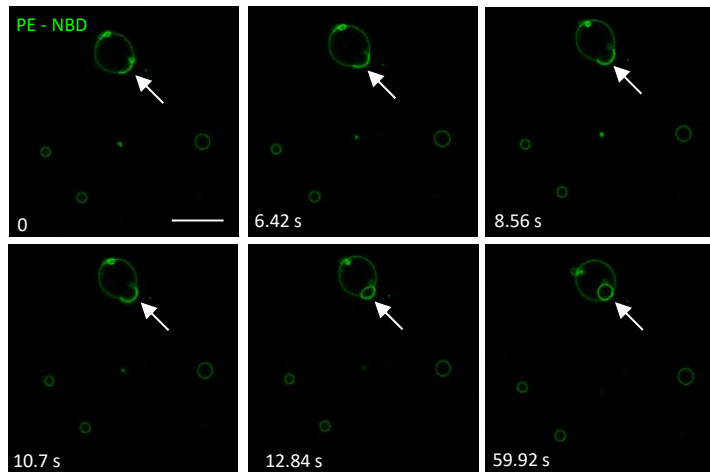
**C**



**E**



**D**



**F**

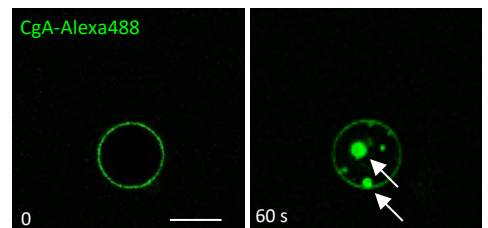


# Figure 4

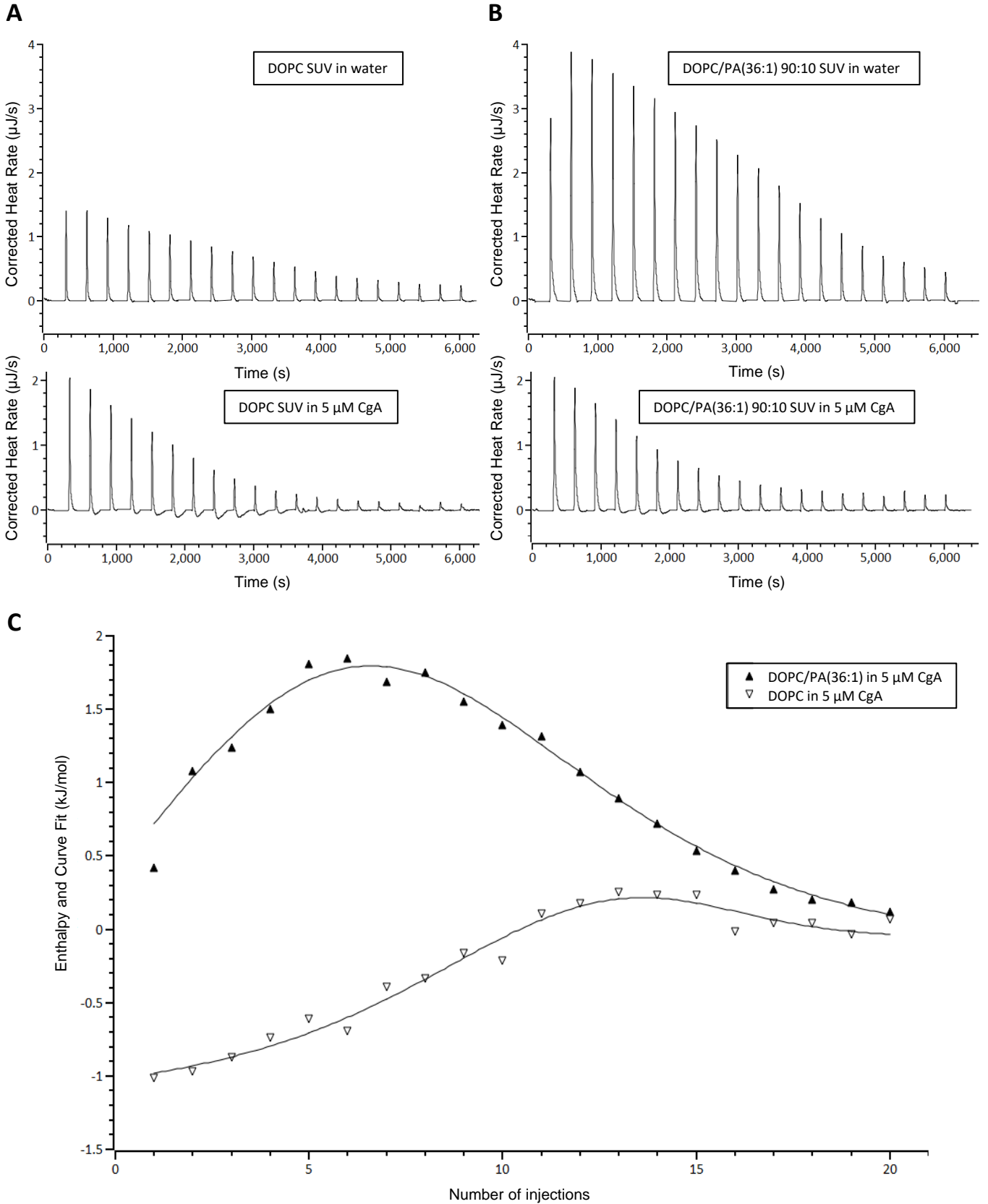
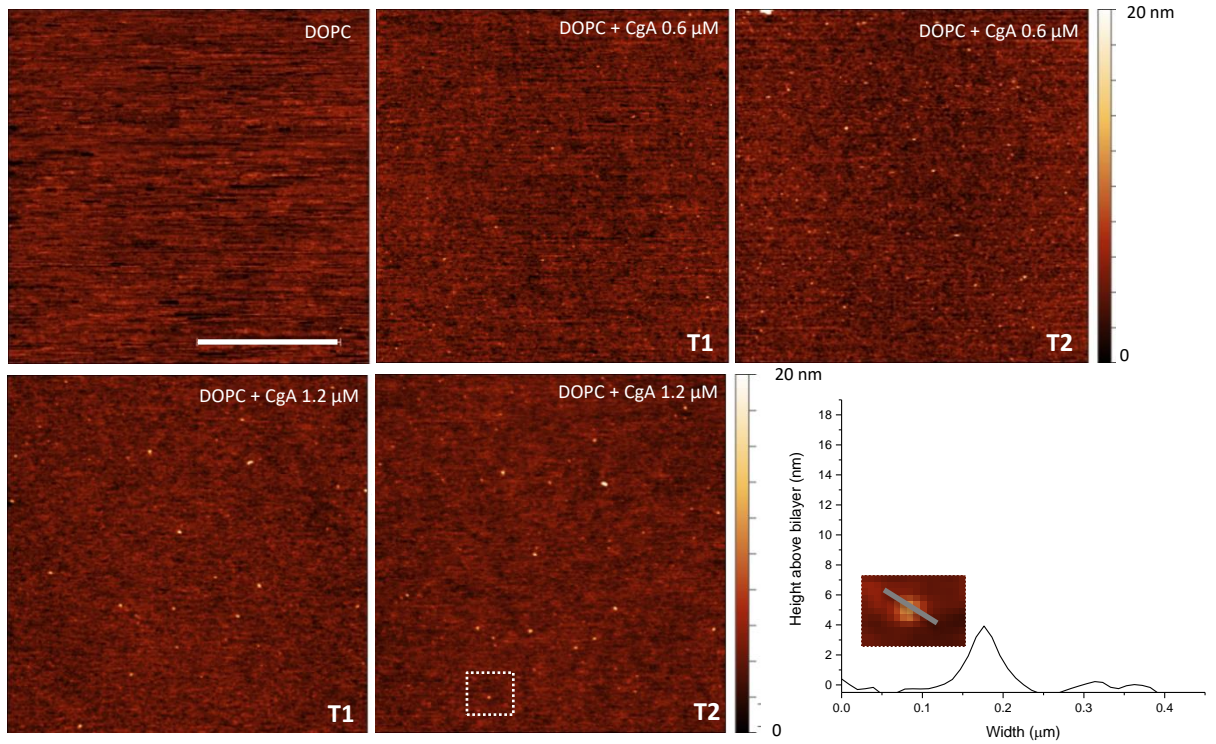


Figure 4

# Figure 5

A



B

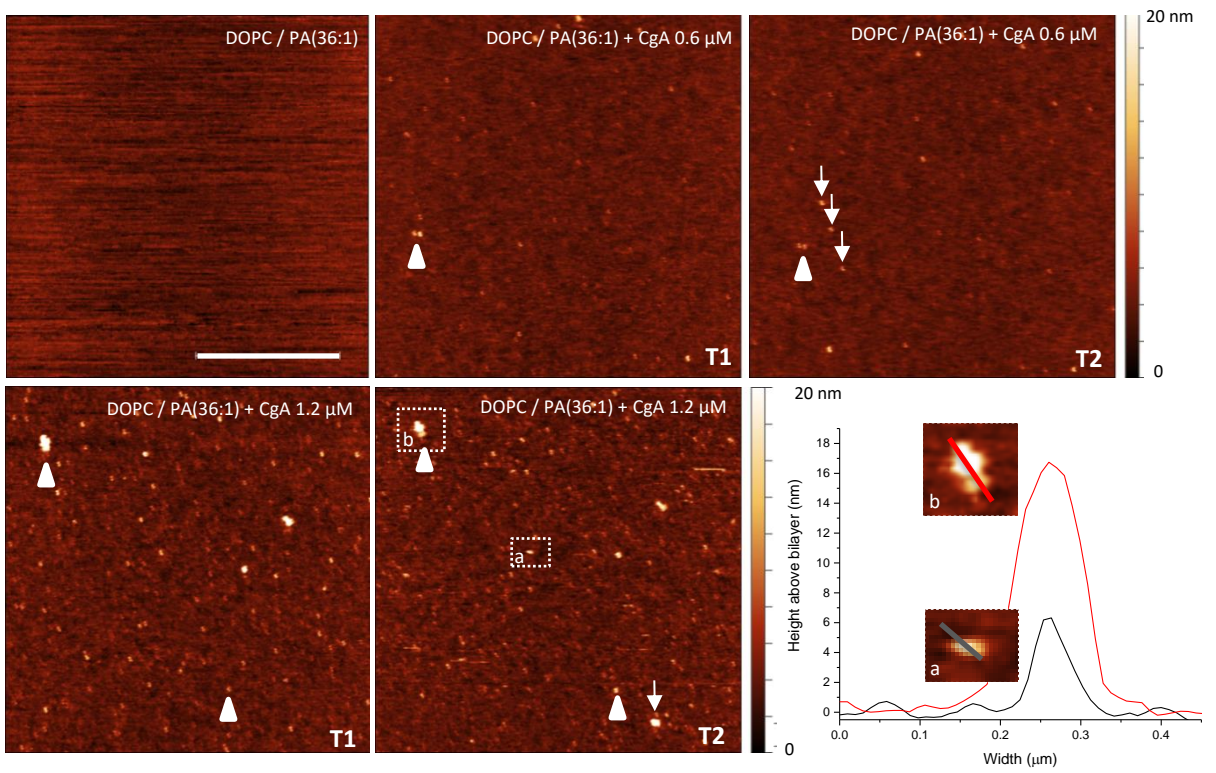
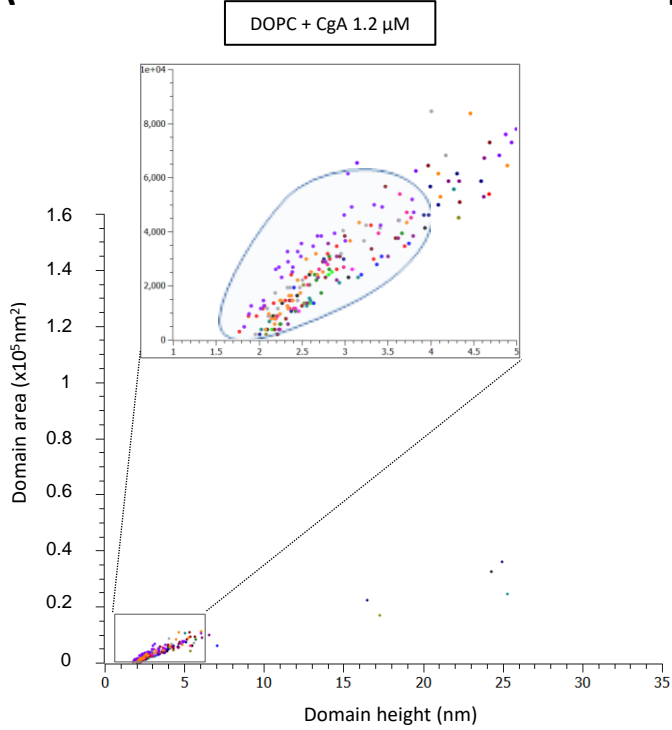


Figure 5

# Figure 6

**A**



**B**

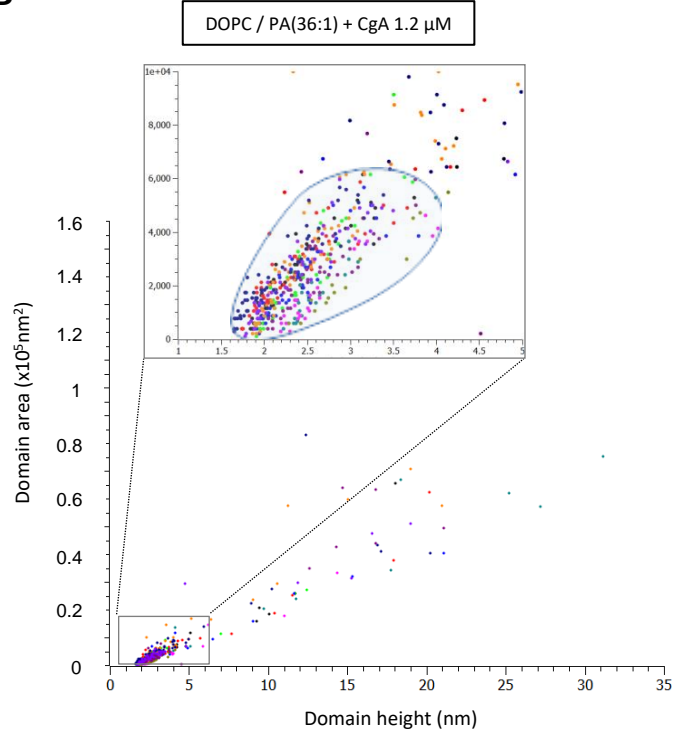


# Figure 7

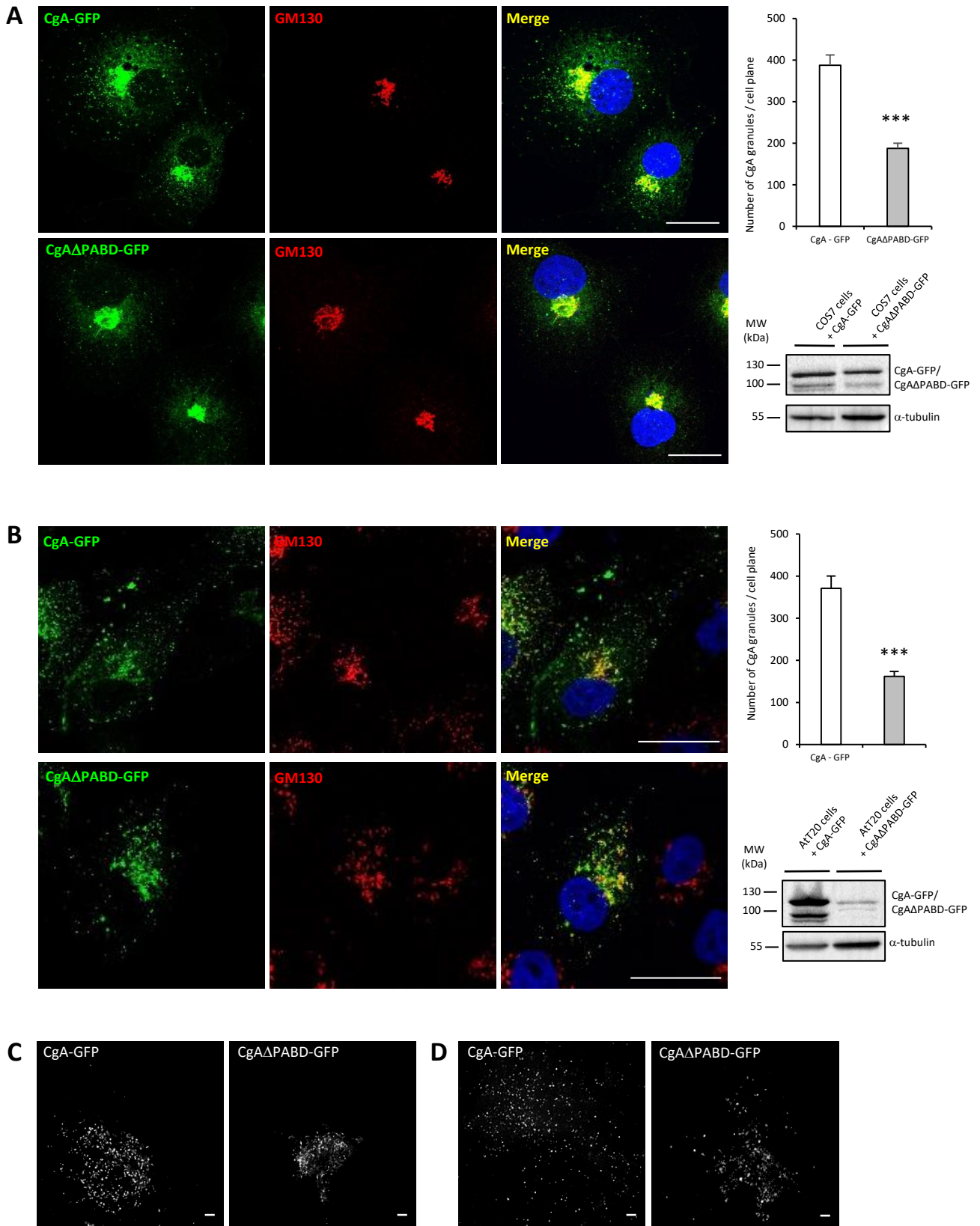


# Figure 8

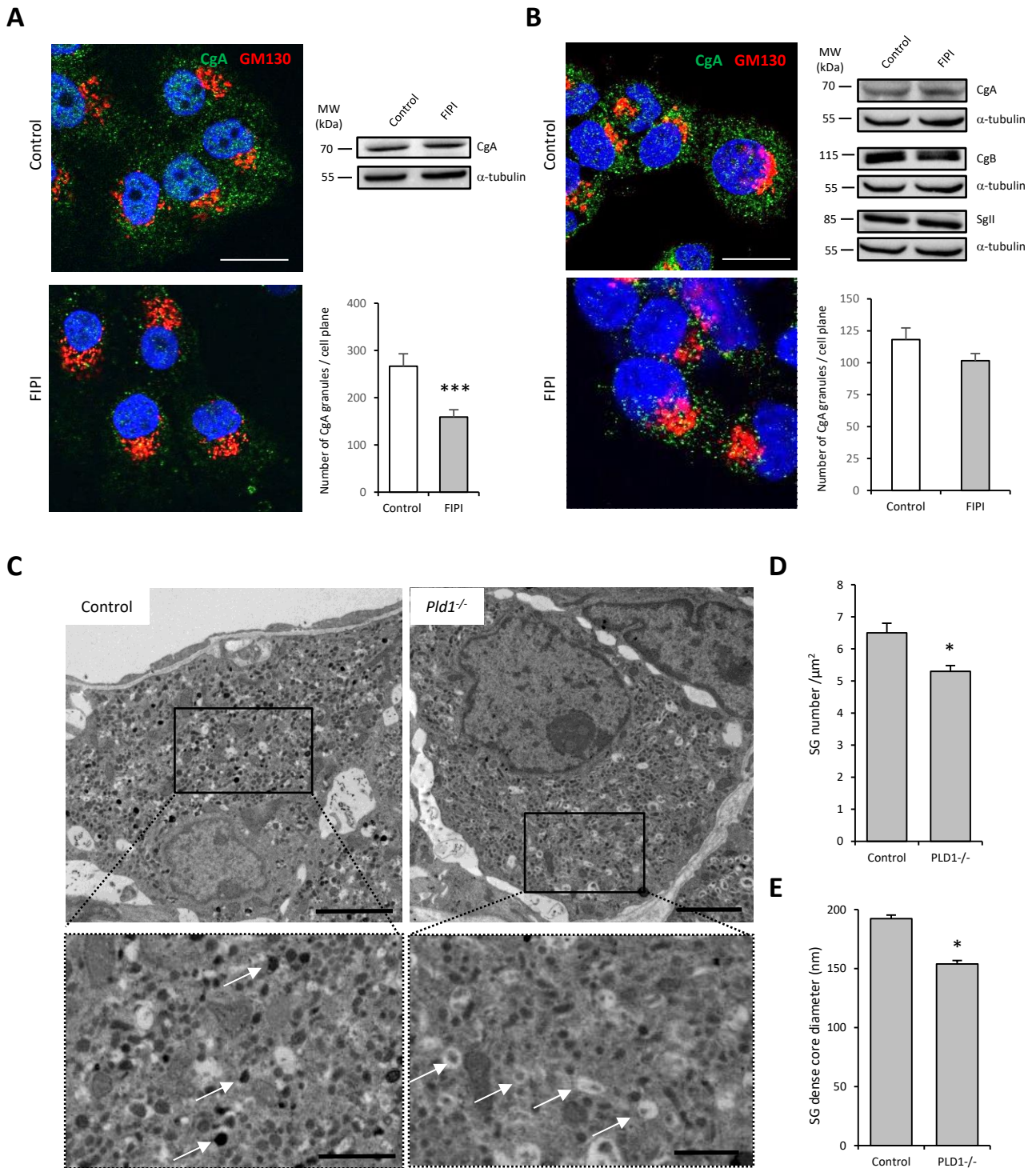


Figure 8

## 1 SUPPLEMENTAL LEGENDS

### 2 Supplemental figure 1.

3 A Enrichment of secretory granule membranes from COS7-CgA cells by subcellular  
4 fractionation using centrifugation on sucrose gradient. Each fraction was collected and  
5 analyzed using SDS-PAGE and SG antibody (anti-RV29.4(CgA), 70 kDa). Surrounding  
6 fraction was selected for lipidomic analysis.

7 B Enrichment of Golgi membranes from COS7 and COS7-CgA cells by subcellular  
8 fractionation using centrifugation on sucrose gradient. Each fraction was collected and  
9 analyzed using SDS-PAGE and immunoblotting with antibodies raised against ER (anti-  
10 CALR, 70 kDa), mitochondria (anti-GLUD1, 55 kDa), *cis*-Golgi (anti-GM130, 130 kDa),  
11 and *trans*-Golgi (anti-golgin 97, 97 kDa). Surrounding fractions were selected for lipidomic  
12 analysis.

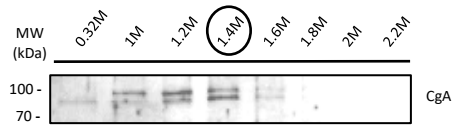
13 **Supplemental figure 2.** Imaging of CgA-GFP positive vesicles in fixed COS7 cells through  
14 confocal light scanning microscopy (CLSM) (A) and deconvoluted time-gated STED  
15 nanoscopy (STED + Deconvolution) (B). While GFP-CgA-positive structure is described as a  
16 single object through CLSM, “STED + Deconvolution” approach reveals the existence of two  
17 vesicles (blue arrows). (C) Improvement of lateral resolution (full width at half maximum,  
18 FWHM) and signal to noise ratio (SNR) through “STED + Deconvolution” strategy. An  
19 intensity profile was measured along a segment drawn on ten vesicles (yellow arrows) and  
20 diameter was determined at full width at half maximum (FWHM). Noise (blue squares) and  
21 Signal (red circles) were measured in 5 different positions in (A) and (B). Through “STED +  
22 Deconvolution” strategy, vesicle diameter is divided by three and SNR is increased sixfold.  
23 (D) Graphic representation of the increase in lateral resolution obtained through “STED +  
24 Deconvolution” strategy. An intensity profile was measured along a segment and adjusted by  
25 using a Gaussian fit. While CgA-GFP positive structure is described as a single object through  
26 CLSM (broken line), “STED + Deconvolution” approach reveals the existence of two vesicles  
27 (full line).

28 **Supplemental video 1.** Distribution of fluorescence around DOPC/PA/PE-NBD GUVs  
29 before CgA addition is homogenous. Confocal live-cell imaging of GUVs containing PE-  
30 NBD (green) was registered over a period of 1 min. Still images are shown in Fig. 3C.

31 **Supplemental video 2.** Distribution of fluorescence concentration before membrane  
32 deformation of DOPC/PA/PE-NBD GUVs triggered by 2  $\mu\text{M}$  CgA addition is not  
33 homogenous. Confocal live-cell imaging of GUVs containing PE-NBD (green) was registered  
34 over a period of 1 min. Still images are shown in Fig. 3D.

35

**A**



**B**

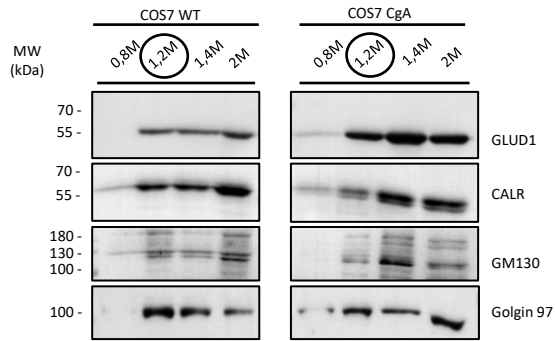
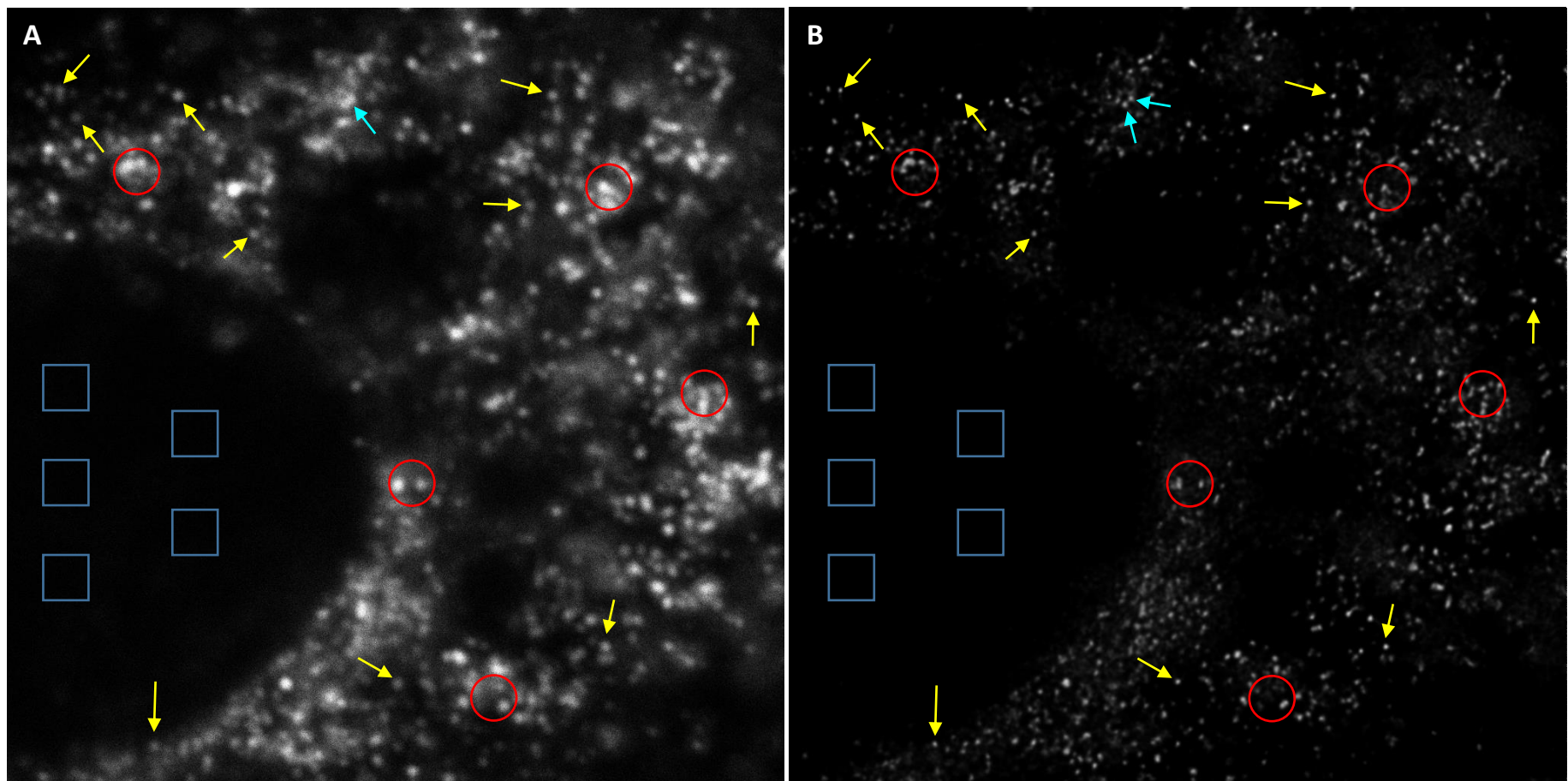


**Figure S1**



**C**

	FWHM (nm)	SNR = $\frac{\text{Signal}}{\text{Noise}}$
CLSM	$230 \pm 17$	$38 \pm 5$
STED + Deconvolution	$80 \pm 9$	$226 \pm 6$

**D**

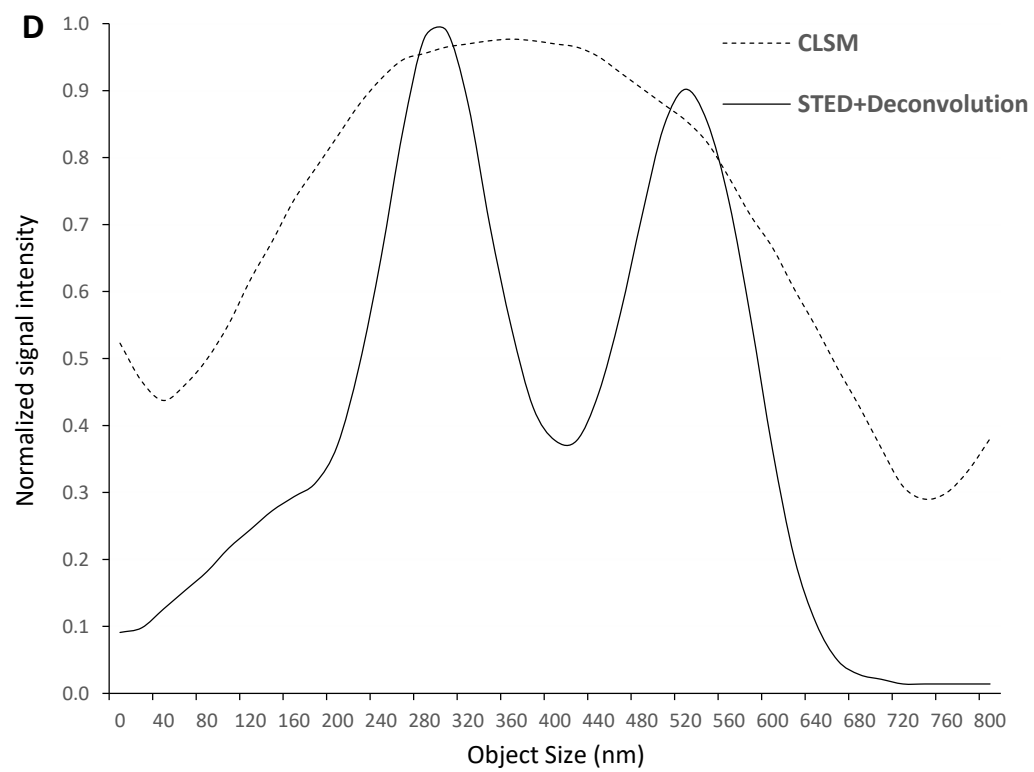


**Figure S2**